Atmospheric
Chemistry
and Physics

Supplement of

A comprehensive characterization of ice nucleation by three different types of cellulose particles immersed in water

Naruki Hiranuma et al.

Correspondence to: Naruki Hiranuma (nhiranuma@wtamu.edu) and Ottmar Möhler (ottmar.moehler@kit.edu)

Supplemental Information

S.1. Particle and Residual Size Distribution Measurements

Particle size distributions of all three cellulose types over the range from 0.01 to 16 μm in diameter (D_p) were characterized in the AIDA chamber. For MCC, we analysed the average size distribution of nine different AIDA experiments (INUIT06_1, 17, 31, 42-46 and 54). During the measurements, we occasionally observed new particle formation events in the vessel (the source is not known). Accordingly, the contributions from these particle formations ($D_p < 50$ nm) were removed and not included in any of our analyses. For FC, two AIDA experiments (INUIT06_6 and 14) were characterized. For NCC, a total of four AIDA experiments (INUIT08_6, 7, 9 and 10) were analyzed to estimate the average size distribution.

For particle injection, dry ground MCC and FC were injected directly into the AIDA chamber using the rotating brush generator (PALAS, RBG1000). Unlike MCC and FC, wet particle generation (dispersion of 0.14 wt% NCC suspension by means of a compressed air atomizer) was employed for NCC. A custom-built atomizer, which is similar to TSI 3076 but without a vertical orifice and with an additional liquid drain bottle independent of an aqueous liquid feeding bottle (*Wex et al.*, 2015), was used for atomization. When we change the sample type examined, all components of a rotating brush generator were disassembled, washed with distilled water and dried in a drying oven to prevent carryover of sample residues into the next sample. Prior to each particle loading, aerosol-free dry synthetic air was passed through the RBG for >30 minutes. We confirmed that the background aerosol concentration was typically ~0.1 cm^{-3} in the AIDA vessel.

After the completion of injection, number and size of polydisperse cellulose particles were measured using a scanning mobility particle sizer (SMPS; TSI Inc., Model 3081 differential mobility analyzer, DMA, and Model 3010 condensation particle counter, CPC) and an aerosol particle sizer (APS; TSI Inc., Model 3321). With given combination, a wide range of size measurements (0.01 to 16 μm assuming all particles are spherical) was realized. A unit dynamic shape factor (DSF, H15a) and the particle density values reported in **Table 1** were used to obtain the geometric-based volume equivalent diameter (D_{ve}) from an APS. We note that our size distribution measurements were carried out only prior to the AIDA expansion experiment since both an SMPS and an APS were pressure sensitive and not able to run while altering sampling pressure in the chamber vessel.

Size distributions of suspended residuals derived from 5 μL of 0.03 wt% suspension were characterized using a scanning electron microscope (SEM, FEI, Quanta 650 FEG). With given concentration and droplet size, we simulated the condition of >100 particles contained

in a single droplet, which is unique in the aqueous suspension experiments as compared to the dry dispersion measurements (i.e., presumably single particle per droplet condition). To minimize the inclusion of aggregates in the bulk suspension, we placed the bulk suspension in an ultrasonic bath (>40 kHz) for ~15 min prior to generating a droplet. Followed by pipetting a

5   5 µL droplet containing cellulose materials on 47 mm membrane filters (Whatman® Nuclepore™ Track-Etched Membranes, 0.2 µm pore size), all water content on the membrane filter was removed under a quasi-vacuum condition in a SEM chamber. After that, their residual size distributions in 2-D area equivalent diameter (D_a, >0.3 µm) were measured by assessing the Everhart-Thornley Detector (ETD) images. With this methodology, we conducted

10   the below-the-lens image acquisition for a total of 3,761, 371 and 610 residuals of MCC, FC and NCC, respectively. The method used to derive SEM-based specific surface area (SSA) using residuals from 0.03 wt% suspension droplets is valid. At this concentration, the SSA of residuals is almost same as that of bulk dry powders (not shown). We confirm this for both MCC and FC. Note that, as the NCC sample is available only in a water-suspended form, we

15   cannot conduct the dry powder versus residual comparison for NCC. Drying suspensions out will cause particles to be drawn together into aggregates. Nonetheless, our SEM observations suggest that the abundance of NCC aggregates is much less as compared to MCC and FC (**Sect. 4.4**). Aggregates may also be present in the suspension as mentioned in **Sect. 4.3.3**. In addition, the degree of agglomeration might be depending on the suspension concertation used to

20   generate droplets. Our attempts to utilize the dynamic light scattering technique (NanoSight NS300, Malvern Panalytical) to measure the cellulose particle size distributions and associated SSA in aqueous suspension as a function of wt% were not successful. Nonetheless, the future study has to follow to constrain the SEM-based SSA and provide more method specific values (see **Sect. 3.1** for more details). A more precise and accurate normalization to the surface area

25   might be the key to constrain the ice nucleation active surface-site density concept.

To ensure the similarity of abovementioned two size metrics (i.e., D_{ve} and D_a) and to further validate the size distribution measurements of an SMPS and an APS, an additional assessment of particle size distributions of dispersed particles was performed. Specifically, we analyzed particles that were collected on the filter directly from the AIDA chamber vessel.

30   Using an SEM, D_a of 503 MCC particles as well as 154 NCC particles collected on either a 47 mm Nuclepore substrate or a copper microscopy substrate were measured to compare to the SMPS/APS size distributions.

Representative normalized surface area distributions (scaled to the total surface areas) of all cellulose particles obtained from the AIDA measurements and droplet residuals

35   are shown in **Fig. S1**. As seen in this figure, the surface area distributions of MCC and FC

particles exhibits its mode diameter (μ) of ~1 μm with a negligible contribution of particles smaller than 0.1 μm diameter (**Figs. S1a** and **S1b**). This dominance of supermicron particles to the total surface area is unique for MCC and FC. In contrast, the NCC particle surface area distribution is dominated by submicron particles with μ ~0.2 μm D_{ve} (**Fig. S1c**).With a minimum particle concentration detection limit of 0.001 cm^{-3}, the largest MCC and FC particle measured by an APS was ~10 μm in D_{ve}. This value is comparable to our previous measurement at MRI-DCECC as shown in Fig. S2 of H15a despite the shift in μ (2.22 μm for previous study). The observed shift may be due to the difference in the cut-size of inertial cyclone impactor stages (D_{50} vary in the range of ~1 to 5 μm). For clarity, the size distribution of MCC measured at MRI-DCECC is overlaid on top of that of AIDA in **Fig. S1a**. Comparing MCC to FC, the mode diameter, μ, of MCC of 1.22 μm is slightly larger than that of FC (μ = 1.13 μm). Interestingly, a similar lognormal distribution width, σ, of ~0.6 is observed for all cellulose particles (0.62, 0.60 and 0.59 for MCC, FC and NCC) regardless of difference in particle generation methods.

As shown in **Fig. S1**, the size of residuals invariably shifts towards the large size for all sample types when compared to that of aerosolized particles. The mode diameter of MCC, FC and NCC residuals (54.24, >65 and 2.68 μm) is at least an order magnitude higher as compared to that of the AIDA chamber-dispersed particles (1.22, 1.13 and 0.21 μm). Our observation of μ > 65 μm for FC suggests that this particular cellulose type tends to agglomerate in water or the original product comes in an agglomerated form in comparison to two other cellulose materials. Moreover, the spectral distribution width of residuals is a lot wider (1.26 and 0.84 for MCC and NCC, respectively) when compared to that of particles (0.62 and 0.59 for MCC and NCC, respectively). Further, the resulting ratio of the total surface to the total mass of residuals (**Table 1**) is up to two orders of magnitude less than that of particles. Overall, these observations suggest that particles in droplets may agglomerate in the presence of multiple particles in a single droplet, altering surface properties (i.e., *SSA*) and perhaps IN efficiency (*Emersic et al.*, 2015; *Beydoun et al.*, 2016).

In addition, our results of comparing D_{ve} to D_a (not shown) indicate the similar size distribution parameters (μ_{MCC} ~1.87 μm D_a and μ_{NCC} ~0.29 μm D_a) regardless of difference in particle generation methods. Though the spectral widths were slightly narrower (σ_{MCC} ~ 0.49 and σ_{NCC} ~ 0.40), observed similarity verifies the validity of our size distribution measurements.

S.2. Chemical Composition

Single particle mass spectra of our cellulose samples are now presented (in **Sects. S.2 and S.3**) for discussion of the difference between dry and wet particle generation and impurities tests. Single particle mass spectra of dry dispersed FC and MCC particles in the size

range between 200 and 3500 nm were measured in the laboratory using the Aircraft-based Laser ABlation Aerosol Mass spectrometer (ALABAMA, *Brands et al.*, 2011). The averaged mass spectra of both cellulose types are shown in **Fig. S2**. The mass spectra of the dry dispersed particles show high signals of anions at mass-to-charge ration, m/z, of -45 (HCO_2), -59

5   (CH_3COO) and -71 ($C_3H_3O_2$). These are typical markers for biomass burning particles, especially levoglucosan $C_6H_{10}O_5$, 1,6-anhydro-*β*-D-glucopyranose (*Silva et al.*, 1999). Levoglucosan is an anhydrous sugar formed from the pyrolysis of carbohydrates, such as naturally occurring starch and cellulose (*Madorsky et al.*, 1959; *Lakshmanan et al.* 1969). Thus, it is not surprising that the mass spectrum of cellulose particles resembles that of levoglucosan. The above

10   mentioned marker ions should therefore be regarded as general markers for plant-related material and are not unique to levoglucosan or cellulose. Now for the cations, the prominent ions are found on the peaks at m/z 19 (H_3O^+), 27 (Al^+ or $C_2H_3^+$), 39 (K^+), 43 (AlO^+, $C_2H_3O^+$, or $C_3H_7^+$) and 56 (Fe^+). The presence of some ions, such as Al, K and Fe, may indicate contamination of the sample.

15   A more detailed analysis of the individual mass spectra revealed several distinct particle types. Using a combination of fuzzy clustering (*Hinz et al.*, 1999) and the marker peak search method based on the above mentioned and further characteristic ions, we found that ≈75% of FC particles contained the characteristic marker peaks. The average mass spectrum of these FC particles is shown in **Fig. S2a**. The remaining 25% of the particle mass spectra

20   showed similar cation spectra but the anions were dominated by signals of elemental carbon (C_n^-). This may be due to a stronger fragmentation of the cellulose molecules or due to other effects. Previous studies have identified at least 37 different compounds in products of cellulose pyrolysis (*Schwenker and Beck*, 1963). Further, those ions in the remaining 25% of the spectra may indicate aluminosilicates that could be a contamination of the sample. The

25   source of these impurities is not known. Two potential sources include the manufacturing process (e.g., controlled acid hydrolysis during the mechanical extraction of natural fibers) and/or contamination from ambient lab air. Similar results were obtained for dry dispersed MCC cellulose particle (See **Fig S2b**). Briefly, approximately 60% of the mass spectra were clearly identified by means of the above mentioned marker peaks. The remaining mass spectra

30   show again the C_n pattern, possibly indicating higher fragmentation, as well as the aluminosilicate contamination.

To compare properties of MCC particles generated by nebulization and dry dispersion, a single particle mass spectrometer (miniSPLAT), a Centrifugal Particle Mass Analyser (CPMA), and a Scanning Mobility Particle Sizer (SMPS) (*Zelenyuk et al.*, 2015; *Alexander et al.*, 2016)

35   were used to measure the aerosol particles vacuum aerodynamic and mobility diameters (d_{va}

and d_m respectively) of mass-selected MCC particles, their mass spectra and effective densities. The "nebulized" cellulose particles were generated by nebulizing a 0.06 wt% suspension using PELCO all-glass nebulizer (14606, Ted Pella, Inc.) and dried through a diffusion dryer prior to characterization. The "powder" particles were generated by powder dispersion using the TOPAS Solid Aerosol Generator (SAG 410) with the spoon method, where small volumes of dry cellulose sample are dispersed by placing it on a spoon and holding it under the ejector.

The results of these measurements are shown in **Fig. S3**. As shown in **Fig. S3a**, for a given mass and, thus, for a given volume equivalent diameter (d_{ve}), the nebulizer-generated MCC particles have smaller mobility diameters when compared to the dry powder population. In contrast, the nebulized MCC particles have larger d_{va} than the dry powder ones (**Fig. S3b**). Such behavior indicates that MCC particle generated by dry dispersion are more aspherical and have larger dynamic shape factors than nebulizer-generated particles (*Alexander et al.*, 2016; *Beranek et al.*, 2012). Consistently, we find that the full width at half maximum (FWHM) of the d_{va} distributions for mass-selected MCC particles generated by dry powder dispersion are broader than those observed for nebulizer-generated particles with the same mass, signifying the presence of more aspherical particles and particles with distribution of shapes as discussed in detail in separate publications (*Alexander et al.*, 2016; *Beranek et al.*, 2012). As an example, data shown in **Fig. S3b** and the material density of 1.5 g cm^{-3} yield average free-molecular regime dynamic shape factors of 2.20 and 1.96 for dry powder dispersion and nebulizer-generated MCC particles, respectively. The d_{va} measurements of size-selected particles can also be used to calculate the average effective densities of the nebulizer- and dry powder-generated particles, shown in **Fig. S3c**. The figure shows that at least across the examined size range (d_{va} and d_m <450 nm) the calculated effective densities appear to be independent on the particle size (**Fig. S3c**), implying homogeneous physical properties. The average effective density of the nebulizer-generated MCC particles (1.16 ± 0.05 g cm^{-3}) is higher than the average effective density of dry powder-generated particles (0.96 ± 0.03 g cm^{-3}), pointing to the relative abundance of compacted, less aspherical and/or less porous particles in the nebulized population. However, both effective densities are lower than the bulk material density (1.5 g cm^{-3}), indicating that both types of particles are aspherical and/or have voids. Clearly, the micrographs of cellulose particles indicate their aspherical elongated appearance with substantial amount of surface structures (Figs. S1 and S3 of H15a).

Finally, **Fig. S3d** presents the comparison of the average mass spectra of nebulizer- and dry-generated MCC particles, acquired by miniSPLAT. The mass spectra of the MCC particles generated by dry dispersion were dominated by C$^+$, CO$^+$, CO$_2^+$, C$_2$O$_2$H$^+$, C$_2$O$_3$H$^+$, O$^-$,

C_2H^-. The mass spectra of the MCC particles generated by nebulization of aqueous cellulose suspension exhibited additional peaks (i.e., Na^+, K^+), most likely from the trace-level metal impurities in the water. Note that the high relative intensity of these peaks in *all* mass spectra of individual nebulizer-generated MCC particles are due to high ionization efficiencies of the

5   alkali metals in single-particle mass spectrometers like miniSPLAT and ALABAMA. While the presence of these trace metals in nebulizer-generated MCC particles, presumably will have negligible effects on IN measurements, the significant differences in shape and morphology of nebulizer- and dry powder-generated MCC particles may affect their IN activity.

S.3. Tests to Investigate Impurities

10   We characterized the samples in more detail than what is reported by what the manufacturers reported. One of the weaknesses of the indirect technique validation at multiple venues is the difficulty to ensure sample purity and stability during distribution and measurement at each institute. Impurity inclusions are often uncontrollable partly because each team treats the samples differently for necessity and known reasons (see the **Manuscript Sect. 3.1**). Potential

15   sources of contaminants include organic gases covering the substrate's surface or the interaction of volatile organic compounds (VOCs) at the vapor-liquid interface (*Whale et al.*, 2015). Besides, several previous studies have reported the dissolution behavior of contaminants (e.g., siloxane and sodium containing materials) from the standard apparatus, such as conductive tube and glassware in water, and even ultra-pure water itself (e.g., *Yu et*

20   *al.*, 2009; *Timko et al.*, 2009; *Bilde and Svenningsson*, 2004).

Though it is hard to identify the source of any potential contaminations and isolate the possibility of sample impurity from other sources and artifacts, such as apparatus and procedures used for solution preparation or sample dispersion, the INUIT group has made an effort to ensure the quality and purity of the samples. The laboratory test results from two

25   electron microscopy groups (KIT and MRI) are discussed in the following sections.

In the Laboratory for Electron Microscopy at the Karlsruhe Institute of Technology, we tested the purity of MCC and FC powders (>0.4 µm), transported back and forth between the U.S. and Europe, using a SEM (FEI, Quanta 650 FEG). In this test, we placed bulk cellulose powders on 47 mm membrane filters (Whatman® Nuclepore™ Track-Etched Membranes, 0.2

30   µm pore size) followed by the sputter coating process to cover cellulose particles with a conductive carbon layer. Subsequently, the coated-membranes were placed in a SEM chamber and exposed to an electron beam to assess the brightness of individual particles with a backscattered electron detector (contrast/brightness = 88.8/74.2) and their elemental compositions with an energy dispersive X-ray (EDX) detector. At the end, this assessment

allows for isolation of non-carbonaceous materials (e.g., dusts and metals) from the other materials according to the brightness contrast (if there are any). With this methodology, a total of 5637 particles (3898 MCC and 1739 FC particles) were analyzed and impurity inclusions of less than 0.25% were identified. This number is nearly equal to the impurity fraction in MCC of 0.28%, which is reported in *Ohwoavworhua and Adelakun* (2010). A few contaminants identified in our cellulose samples are copper/aluminum oxide, quartz, chromium sulfate/sulfide, sodium chloride, non-aluminosilicate salt, pure chromium and lead. Note that no aluminosilicates were found. Except lead (*Cziczo et al.*, 2009), all other compounds are known to have negligible ice nucleation activities at $T > $ -25 °C and at least an order magnitude lower n_s(T) compared to H15a-MCC as suggested in our previous AIDA tests and other studies (e.g., *Archuleta et al.* 2005; *Steinke*, 2013; *Hiranuma et al.*, 2014; *Atkinson et al.*, 2013).

A complementary impurity analysis was carried out using another SEM-EDX (SU-3500, Hitachi) and a transmission electron microscope (TEM, JEM-1400, JEOL) at MRI, Japan. A total of 123 SEM images of MCC and FC powders (<10 µm) as well as a few TEM images of NCC that has the geometry of several tens nanometer with 500-800 nm length were analyzed. There were no notable contaminants except some expected elements, such as sulfur and sodium, which possibly stemmed from the manufacturing process of NCC [i.e., $(C_6H_9O_5)_n$ $(SO_3Na)_x$].

In some cases, bulk particles may break apart into fragments, and those fragments may appear in an analytical instrument (e.g., single particle mass spectrometer) with a high detection sensitivity and efficiency. For MCC, the total fraction of contaminants, which may cumulatively derive from any experimental procedures (e.g., sample transport, treatment and impurity), is ≤3%, as formerly reported in H15a. Ostensibly, these contaminants may have emanated from the brush generator or the AIDA chamber walls. Nonetheless, blank reference AIDA expansion experiments (i.e., background expansion cooling measurements without aerosol) suggest that impurities negligibly impact the ice nucleation activity of cellulose at heterogeneous freezing temperatures of $T > $ -33 °C. In brief, we examined the immersion mode IN activity of 'sample blanks' injected through running a blank brush generator for >60 min in the chamber. Our SMPS/APS measurements showed that the blank injection provided <23 cm^{-3} of particle concentration (equivalent to <2 μm^2 cm^{-3} surface), and >80% of background particles are smaller than 250 nm. Our experimental results (2 independent expansions; INUIT03_2 and _3) indicated no ice observed at $T > $ -33 °C. Further discussion regarding impurity is beyond the scope of the concurrent study.

S.4. Descriptions of Ice Nucleation Techniques

A summary of quantifiable parameters involved in dry dispersion experiments is given in **Table S1**. For dry dispersion measurements, both monodisperse and polydisperse aerosol populations were used to examine ice nucleation abilities. Monodisperse particles were size-selected by differential mobility analyzers (DMAs, manufacturer information are given in **Table 1**), and selected sizes ranged from 320 to 800 nm in mobility diameter depending on the aerosol and ice detection sensitivity of the technique. For MCC and FC, polydisperse particles were predominantly in the supermicron size range, but the particle size distributions varied between techniques as the mode diameters ranged from ≈1 to 2 μm. The measured geometric *SSA* values correspondingly deviated for up to an order of magnitude for all cellulose sample types, indicating various size distributions. Similarly, the size of supercooled droplets ranged from 2.6 to 90 μm, and the ratio of the aerosol size (i.e., mode diameter) to the droplet size also ranged over two orders of magnitude (0.0036-0.5). Furthermore, a total number of droplets examined per experiment varied over two orders of magnitude (100-10,000) depending on the technique. Above all, the temperature uncertainty of the dry dispersion techniques was fairly small (within ± 1 °C) despite of variation in cooling rate (0.9-2.8 °C min^{-1}), ice nucleation time (0.2 s – 15 min) and a difference in the way of determining the fraction of frozen droplets. Concerning the latter, most of the dry-dispersion methods measure the concentration of ice crystals and separately determine the particle concentration, assuming that for immersion freezing measurements the conditions chosen in the instrument cause all particles to be activated to droplets. This yields the ratio of measured pristine ice crystal concentrations to the particle concentration, the so-called "activated fraction"(*AF*) as described in *Burkert-Kohn et al*. (2017). Others look at the entirety of all droplets and check how many of these are frozen, determining a "frozen fraction" (*FF*), the latter being done e.g., for LACIS (*Burkert-Kohn et al*., 2017), but generally also for all aqueous suspension methods. It is important to note that CFDCs may expose particles to different humidities and/or temperatures in chamber geometry; therefore, *AF* = 1 is not achieved because not all particles are activated into the droplets in CFDCs (*Garimella et al*., 2017; 2018). However, it should be pointed out that recently systematic differences were described when comparing CFDC (continuous flow diffusion chamber) methods with other immersion freezing methods (AIDA and LACIS), (*DeMott et al*., 2015; *Burkert-Kohn et al*., 2017). In these studies, simultaneous measurements at the same measurement location were done, and CFDCs yielded lower results by roughly a factor of 3 for conditions where all particles should activate to droplets in the instruments.

Table S2 provides a summary of quantifiable experimental parameters of the aqueous suspension techniques. A majority of the techniques used the bulk cellulose samples, containing larger particle sizes as compared to dry dispersed ones. In association with their large grain size, bulk samples exhibited smaller *SSA* than dry dispersed ones (**Table 1**). Note that the SEM-based *SSA* values from **Table 1** were used for the $n_{s,geo}(T)$ estimation of most bulk-based measurements. Two exceptions were the <10 µm particles examined with NIPR-CRAFT and dispersed particles collected on filters and scrubbed with deionized water for FRIDGE-CS. The results of these unique size-segregated measurements were compared to the bulk results (see **Manuscript Sect. 4.3**).

The volume of water used in each aliquot in aqueous suspension techniques was in many cases much larger than in the volume of the droplets generated in dry dispersed techniques. The ratio of the aerosol mass (i.e., mass equivalent diameter) to the droplet mass of the aqueous suspension subset was on average much smaller (for less than an order of magnitude) as compared to that of the dry dispersion subgroup. Therefore, the solute concentration per drop in the wet suspension experiments was greater than in the dry suspension experiments. This might be important since solutes have been shown to both enhance and suppress ice nucleation even in very dilute solutions (Kumar et al., 2018; Whale et al. 2018). An exception was WISDOM, which used <100 µm droplet diameters (<0.5 nL volume). A total number of droplets examined per experiment was several hundred at the most and typically smaller than that of dry dispersion techniques. The total surface area probed was, however, much larger in aqueous suspension methods, resolving much warmer temperatures. Temperature was well-controlled in these methods. For example, similar to the dry dispersion measurements, the temperature uncertainty was fairly small (within ± 1 °C) regardless of variations in cooling rate (0.4-2.0 °C min^{-1}). As seen in **Table S2**, the weight percent of particle suspensions varied over five orders of magnitude (10^{-5} to 1 wt%) to access a wider freezing temperature range. On the other hand, the resulting $n_{s,geo}(T)$ uncertainty of >20% and slope parameter of $n_{s,geo}(T)$ spectrum (0.2 < Δlog($n_{s,geo}$)/ΔT < 0.47) exhibited large deviations as can be seen in **Table S2**. The Δlog($n_{s,geo}$)/ΔT value of this subgroup (≈0.34) was on average larger than the dry dispersion subgroup (≈0.18). More detailed discussion of quantifiable parameters in **Tables S1 and S2** are provided in **Sect. S.9.2.**

Nominal method descriptions of dry dispersion and wet suspension techniques are listed in **Tables S3** and **S4**. Information given in these tables include the impactor type used while dispersing cellulose materials (if employed), background correction method, ice detection method, valid data range, sample pre-treatment, water type and a description of the suspension solution while generating droplets/vials.

Background correction methods vary amongst the dry dispersion methods (**Table S3**). For CFDCs (CSU-CFDC, INKA and PNNL-CIC), background INP concentrations estimated by taking measurements through a filter for before and after the sample period were accounted. For controlled expansion cloud-simulation chamber (CECC) and dynamic DECC (i.e., AIDA and MRI-DCECC), an expansion without aerosols in the vessel, namely blank expansion (*Hiranuma et al.*, 2014), was conducted to confirm negligible background non-IN active particle concentrations prior to the experiment. For diffusion cells (DFPC-ISAC and FRIDGE-default), background INP concentrations on blank filters/wafer were subtracted from the actual ice crystal concentrations of loaded filter/wafer.

S.5. Surface Structure of Cellulose Samples

Cellulose particles consist of a complex porous morphology with capillary spaces between the nanoscale fibrils (H15a). These surface structures may make the surface accessible to water and induce a varying sensitivity to heterogeneous ice formation (*Page and Sear*, 2006; *Subramanyam et al.*, 2016; *Kiselev et al.*, 2017). To better understand the nanoscale surface morphology of cellulose materials, surface structures of all three cellulose materials were characterized using a scanning electron microscope (SEM, SU-3500, Hitachi). To minimize the deformation of a specimens' surface by the intense electron beam bombardment, we purposely used an acceleration voltage of 5 keV and a working distance of 5 mm in a low vacuum mode (50 Pa). Dry MCC and FC particles from the batches were sprinkled over a carbon tape substrate. A number of SEM images (61 MCC and 62 FC particles) were afterwards taken for randomly selected <10 µm particles with an Ultra Variable Pressure (UVD) detector at 2560 ×1920 pixel resolution. After the micrograph image acquisition, our images were analyzed to estimate the line structure density and size distribution of defects on the surface of all 123 particles. For the image processing, background signals from the carbon tape substrate in the proximity of target particles were first removed by subtracting threshold intensities between particles and the background. Thus, particles were distinguished from the carbon tape by choosing an appropriate threshold value of image intensity to yield binary images (*Adachi et al.*, 2007 and 2018). Followed by the background correction, line structures on the particle surfaces were clipped. These line structures were typically brighter than the other areas because of their edge effects on the UVD images. Line structures with >0.25 µm were chosen to characterize the particle surface, i.e., surface features with <0.25µm were ignored as noise because of a lack of SEM image resolution. Afterwards, the length of individual line structures extracted from the original SEM image was measured over the entire grid along both X and Y axes. No major image distortion was observed and, hence, no

corrections for curvature were applied. Lastly, the distributions of the length were integrated for particle type (i.e., MCC and FC) to assess the overall size distributions of these surface linear peaks. Consequently, surface areas of all 123 particles were also measured from SEM images, and the abundances of the line structures were scaled to their surface area measured by SEM.

5   Our attempt to facilitate SEM for NCC surface characterization was unsuccessful since our NCC sample contained fibers smaller than its spatial detection limit (~0.25 μm). We also employed a transmission electron microscope (TEM, JEM-1400, JEOL) to analyze the NCC surface. The NCC sample was diluted with water (0.03wt% NCC) and pipetted onto TEM grids with both formvar and lacey carbon substrates (U-1007 and U-1001, respectively; EM-Japan, 10   Tokyo, Japan). The results of both our SEM and TEM analyses are available below. We will also discuss possible explanations for the observed diversity of data from different techniques in detail below.

A detailed discussion of the samples comparison (surface difference) is given in this sub-section. **Figure S4** shows a representative SEM image and a processed image for MCC. As 15   can be seen in **Fig. S4a**, our cellulose surface possesses substantial amount of line structures and defects that may provide thermodynamically preferential condition to suppress the energy barrier of crystallization and perhaps induce different interactions with water vapor and/or super-cooled water droplets (*Page and Sear*, 2006). Brighter regions of the line structures in **Fig. S4b** correspond to structural peaks whereas darker parts represent troughs 20   on the surface.

Figure S5 shows the surface density of these submicron structures on MCC as well as FC (i.e., a compilation of 61 MCC and 62 FC particles). Interestingly, the lengths of linear peaks are log-normally distributed on both MCC and FC particles with modes of ~0.6 and 0.7 μm, respectively. Moreover, the line structure length of FC particles is slightly larger but less 25   abundant than those of MCC particles. At the mode size, the structure density exceeds 0.4 μm^{-2} (4×10^{11} m^{-2}) for MCC and 0.3 μm^{-2} (3×10^{11} m^{-2}) for FC. Note that there is none for NCC. In addition, we also examined seven of >10 μm MCC particles and confirmed they had similar features as <10 μm particles (not shown).

Figure S6 shows TEM and SEM images of NCC particles at various magnifications. 30   Unlike MCC and FC, there exist no notable surface defects on the NCC surface. As shown in the TEM images, NCC seems to be composed of single fiber with 10s nm width and 500-800 nm length. At a given aqueous concentration (0.03 wt%), some NCC fibers aggregate each other, forming particulate aggregates of >1μm; however, there are less abundant agglomerations as compared to MCC and FC based on our SEM observations (**Fig. S6 e and f**).

Together with our offline characterization of sample physicochemical properties (**Supplemental Sect. S.2**), we observed the presence of considerable amount of surface porosity and line structures on MCC and FC type particles. With a mode size of >0.6 μm, the surface density of these surface structures is estimated to be at least 3 x 10^{11} m^{-2}. This density is almost equivalent to the observed maxima of $n_{s,\text{geo,MCC}}$ (**Table 4**), suggesting these structures may act as ice active sites and may be responsible for heterogeneous freezing, assuming the density of these linear structures correlate with that of pores, acting as ice active sites. In contrast, there is no surface structure observed for submicron NCC as it mainly retains a single fibrous form. Most importantly, our observation suggests that submicron-sized pores that are uniquely abundant on MCC and FC may be, at least partially, responsible for the observed differences in ice nucleation efficiency amongst materials (i.e., $n_{s,\text{ MCC/FC}} > n_{s,\text{ NCC}}$) prescribed in **Manuscript Sect. 4.2**. It is, however, important to note that our method is limited to measure line structures of approximately >0.25 μm. The structures of <0.25 μm are presumably considered as noise because of poor SEM resolution. Though looking into the pore size distribution and the void volume density of the samples below this size threshold is beyond the scope of the current study, it is necessary in the future to carry out a more detailed study in characterizing surface structure by applying a modern surface physisorption characterization tool. It is possible that a capillary condensation of nano-sized pores (i.e., inverse Kelvin effect) occurs, enhancing ice nucleation (*Marcolli*, 2014 and 2017).

S.6. Log Average Supplement

Figure S7 shows the log average of three cellulose materials used in this study (i.e., *T*-binned log average data from **Fig. 1. iv** for MCC, FC and NCC). Reference immersion freezing $n_s(T)$ spectra for MCC (H15a) are also shown (See **Manuscript Sect. 4.1**).

S.7. AIDA Supplement

Figure S9 summarized the AIDA experiments with MCC, FC, NCC01 and NCC02. The figure is provided in support of the statements made in the Section 4.3.8, which is not evident from the compressed Figures in the main text.

S.8. NC State-CS Supplement

Figure S9 summarized the NC State experiments with FC, MCC, and NCC. The figure is provided in support of the statements made in the Section 4.3.18, which is not evident from the compressed Figures in the main text.

S.9. Experimental Parameters

This section addresses the relationship between experimental conditions/parameters and ice nucleation results to find a potential controlling factor of the observed measurement diversity in T and $n_{s,geo}(T)$. Particularly, we discuss the influence of impurities within water towards freezing (**Sect. S.9.1**) and nominal experimental parameters (**Sect. S.9.2**) on our immersion freezing measurements.

S.9.1. Water Freezing Spectra

Heterogeneous nucleation experiments often suffer from unknown ice active contributors or foreign contaminants suspended in supercooled droplets, triggering non-homogeneous freezing at supercooled temperatures ($T > $ -38 °C). Even with high purity water, it is difficult to eliminate the contribution of heterogeneous INPs in water, especially when using droplets on the microliter scale (*Whale et al.*, 2015 and references therein). To our knowledge, only a small number studies have reported their microliter water droplets to produce freezing spectra with negligible artifacts and reproduce freezing temperatures close to the homogeneous limit predicted by CNT [*Tobo*, 2016; *Reicher et al.*, 2018; *Polen et al.*, 2018; *Peckhaus et al.*, 2016; *Fornea et al.*, 2009 – note the data is not shown in *Fornea et al.* (2009)]. To understand the contributions of the impurities within water towards freezing results, we further analyzed the immersion freezing results of various purity grade water used in aqueous suspension experiments.

Figure S10 shows frozen fraction spectra of pure water with different grades and freezing temperatures of background INP per liter in the water. Various freezing temperatures seen in **Fig. S10a** suggest that freezing behavior of the water depends on the droplet size and several types of water purity grades. Clearly, the comparison of background freezing of different droplet volumes (1, 3 and 5 μL) evaluated by WT-CRAFT indicates that larger droplet volume promotes early freezing at high temperatures. Thus, despite unknown source of such an early onset, the probability of undesired INP inclusion seems – as expected – to correlate with individual droplet size. As apparent in **Fig. S10b**, homogeneous nucleation can occur at higher temperatures than -38 °C (*Koop and Murray*, 2016). For instance, 10 μL droplets would possess 50% activation at just below -33 °C with a cooling rate of 1 °C min^{-1}. The WISDOM measurements with 0.6 nL of DI water are consistent with homogeneous nucleation.

The observed heterogeneous freezing of the water may not solely reflect impurity in the water as it is inherently related to other system artifacts, such as variation in heat conduction and droplet T, contribution of a supporting substrate and dissolved foreign gases.

It is also noteworthy that using autoclaved sterile water did not hinder the background droplet freezing on WT-CRAFT, implying negligible biological contribution to the observed water droplet freezing. In addition, it has been shown that the surface on which microliter droplets are supported also introduces background freezing sites, with ultra pure silicon or Teflon surfaces producing less background freezing than a hydrophobic glass surface (*Diehl et al.*, 2001; *Price et al.*, 2018). The characterization of water quality to identify what causes the observed dominant background freezing in deionized water is beyond the scope of our investigation. However, determining the best possible practice to make sure the freezing temperatures of pure water droplets <-30 °C or lower is important in aqueous suspension experiments (*Knopf et al.*, 2018; *Price et al.*, 2018; *Polen et al.*, 2018). For example, using microfluidically generated sub-micro liter drops and proper substrate condition (e.g., where the droplets are completely surrounded by oil and not in contact with the substrate) may be the key (*Tarn et al.*, 2018; *Polen et al.*, 2018). Another key is to check the background freezing on a routine basis. Obtaining absolutely clean water is conceivably challenging. Perhaps, running a control experiment with commercially available HPLC water may provide complementary insight on the inter-system offset. *Polen et al.* (2018) recently evaluated a series of different substrates and water purification strategies to reduce background freezing interference in droplet freezing assays. They propose a series of recommendations regarding experimental methods and data analysis strategies to reduce and properly account for these background freezing interferences. Note that the shift in freezing temperatures in **Fig. S10c** may also in part derive from the deviation in INP detection methods or variation in heat conduction and droplet *T*. A systematic calibration of the temperature sensor (and associated freezing/melting point) would benefit increasing overall accuracy and precision of droplet assay techniques. It is also important to note that the apparent steep increase in INP concentrations for the WISDOM device at temperatures below about -34 °C (**Fig. S10c**) does not imply that the water droplets in these experiments contained numerous INPs. Instead, the observed sharp increase in freezing rates of these rather small (<100 µm) droplets, which might be particle-free, is most probably due to homogeneous ice nucleation. The observation agrees with previous studies of homogeneous ice nucleation in droplets of this size and published homogeneous ice nucleation rates (*Riechers et al.*, 2013; *Ickes et al.*, 2015).

In addition, the differential freezing spectra of the water used suspending cellulose samples can be used to assess the background freezing. The concept and importance of the differential freezing spectra is described in *Vali* (2018) and *Polen et al.* (2018), stemmed from the original concept introduced in Vali (1971). Briefly, the differential freezing, *k*(*T*), can be formulated as:

14

$$k(T) = -\frac{1}{V_d \Delta T} ln\left(1 - \frac{\Delta N}{N_u(T)}\right) \tag{S1}$$

in which $k(T)$ is the differential ice nucleus concentration (L^{-1}), V_d is the individual droplet volume, ΔT is an arbitrary temperature step, ΔN is the number of frozen droplets within aforementioned ΔT, and $N_u(T)$ is the total number of unfrozen droplets at T. Note that ΔT is not the temperature step of the actual measurements, ΔT_m. The study of ΔT could be explored in the future for a detailed quantitative assessment of artifacts including the background INP concentration. In this study, as we address the background correction method of individual techniques in **Tables S3 and 4**, we elect not to report $k(T)$.

S.9.2. Nominal Experimental Parameters

The discussion of the experimental parameters, which may be responsible for the observed diversity of ice nucleation data, is now provided. As seen in **Tables S3 and S4**, experimental procedures are diverse, potentially responsible for abovementioned deviations in quantifiable experimental parameters. For example, the ice detection methods deviate, highly depending on the size and number of supercooled droplets examined. Thus, the standardization of ice detection is important to minimize the measurement diversity. Correspondingly, the false/positive image analysis should be standardized not to miscount half frozen half unfrozen droplets (*Wright and Petters*, 2013). The 8bit mean gray value image analysis procedure introduced in *Budke and Koop* (2015) is ideal and recommended to the new cold stage users. Other emerging technologies (e.g., application of IR to detect the latent heat release and droplet freezing) may become available in the future (*Harrison et al*., 2018). On the other hand, *in situ* methods detecting droplets that were grown on single particles typically use OPCs for ice counting (except microscopy-combined individual freezing observation apparatus, such as EDB, FRIDGE and DFPC-ISAC). Detecting small ice crystals and separating them from droplets of the overlapping optical size range is a challenge *(Vochezer et al*., 2016). In LACIS, a change in depolarization is used to discriminate between frozen and liquid droplets (*Clauss et al*., 2013). A depolarization technique has been implemented in other ice nucleation methods (*Nicolet et al*., 2010; *Garimella et al*., 2016). A new technology of optical scattering methods (e.g., *Glen et al*., 2013; 2014) was recently introduced to improve the small ice detection capability.

S.10. Diversity between Measurement Techniques

Observed deviations could arise from a number of sources. As verified in this manuscript, there are many experimental variables involved in currently available INP measurement techniques, and such a diverse variation seems to yield significant data diversity and limit the instrument validation by distributing any reference bulk materials. To at least qualitatively examine what experimental parameters predominantly generate the $n_{s,geo}(T)$ diversity, the MCC results of a selected number of measurements derived under similar experimental condition were systematically compared. Our results show that two distinct modes of more and less active ice nucleation were found at higher temperatures for dry dispersion and aqueous suspension results, respectively. To further validate the INP measurement instruments using reference INPs in the future, we suggest the following six points:

1) **Working with similarly produced samples:** As described in **Sect. 4.3.7**, our cellulose powders (especially MCC) promptly settle in water. Sampling a filter of size segregated cellulose generated by means of dry dispersion from a large volume chamber after letting supermicron-sized MCC settle out and running it on a droplet freezing assay (e.g., **Sects. 4.3.2 and 4.3.3** DFPC-ISAC and FRIDGE) is important to assure working with the same sample. Otherwise, aerosolising and then doing the ice nucleation experiment versus suspending particles in water might result in different particle populations. Knowing the sample volume of air, V_s, and liquid suspension volume, V_w, we can estimate immersion freezing efficiency of the sample particles in terms of INP concentration per volume of air [$n_{INP} = c_{INP}(T)\left(\frac{V_w}{V_s}\right)$]., which may be a better ice nucleation parameter for the instrument comparison. Additionally, the study of ΔT to understand the $k(T)$ feature (*Vali*, 2018) could be explored for a detailed quantitative assessment of artifacts including the background INP concentration.

2) **Sample stability analysis:** Chemical and structural changes during sample processing (e.g., *Lützenkirchen et al*., 2014) should certainly be considered more carefully. Depending on the aerosolization method, the surface properties can be altered even for the same sample (see **Sect. 2.2**). For instance, the changes in particle size, morphology and hygroscopicity can occur for atomized particles from a suspension of the powder in water, compared to the dry powder (*Koehler et al*., 2009; *Sullivan et al*., 2010). Understanding the effect of alteration in particulate properties on IN (e.g., *Polen et al*., 2016) must be studied in the future.

3) **Interfacial effect characterization:** Since the cellulose is a strong desiccant and absorbs a lot of water from the droplet, pre-exposure to humidified condition may

16

create partially immersed solid-liquid interfacial condition. An effect is viable. For instance, supermicron-sized particles (MCC and FC) partially immersed but half exposed to air may create the interfacial condition preferable for ice formation. This quasi-contact (perhaps also condensation) freezing process may be analogous to the dry dispersion techniques (with different induction time). The future study to visually inspect this mechanism by means of microscopy (*Kiselev et al.*, 2017) and verify it as an atmospherically representative process is an imperative task. Though looking into the stability of the samples is beyond the scope of the current study, it is necessary in the future to carry out a more detailed study in characterizing the saturation level and temperature dependence of specific adsorption-desorption processes at atmospherically relevant heterogeneous freezing temperature range of cellulose at <-4 °C (*this study*) by applying a modern surface physisorption characterization tool. It is possible that the freeze-thawing processes affect stability of cellulose materials due to water uptake, swelling, drying and/or shrinking. It is also desired to carefully look into pre-activation (e.g., *Wagner et al.*, 2016).

4) **Method Standardization:** Standardization of our methods (e.g., ice detection and in particular INP sampling and treatment) may be one route to reduce the prevailing measurement diversity. Evidently, we verified that the aqueous measurements with smaller droplets and less aerosol exerted high $n_{s,geo}(T)$ of cellulose samples (**Sect. 4.3.14**). A similar observation is addressed in *Beydoun et al.* (2016). As atmospheric cloud droplets range over sizes up to some tens of micrometres (*Miles et al.*, 2000), using an atmospherically relevant range of water volume or at least tenth of micro-liter scale may be a key to improve our measurement comparability in the future. Such effort may reduce the diversity in experimental conditions and unify the experimental parameters (e.g., $\Delta \log(n_{s,geo})/\Delta T$). Currently, given parameters are treated as if free variables, certainly contributing to the data diversity. A community-wide effort to quantify nominal characteristics of each technique (e.g., background correction and sample pre-treatment) is another key to achieve more precise and accurate INP measurements (*Polen et al.*, 2018). For future works, aqueous suspension measurements aligned with the protocol are desired. This might warrant the particle size distribution of the steady-state suspension, perhaps similar to what is examined in the cloud simulation chamber experiments. Alternative strategy is to rigorously examine the causes and clearly define the limitations of individual techniques. Nonetheless, we believe a current diversity in techniques is beneficial at least at this

point, in particular because they allow different types of approaches for identifying new INPs.

5) **Active site validation:** One of the biggest uncertainties in the $n_{s,geo}(T)$ concept is the interpretation of particle surface area (H15b). More rigorous understanding of the true surface area of the system by parameterising *SSA* as a function of particle concentration in a drop is a crucial step to constrain the $n_{s,geo}(T)$ concept as this parameter obviously varies amongst experiments as presented in this work (**Sect. 2.1**). Given the size-dependence of $n_{s,geo}(T)$ for MCC discussed in **Sect. 4.3.4**, varying concentration to access a wider freezing temperature range and stitching the $n_{s,geo}(T)$ spectra obtained from different concentrations together may be problematic (*Beydoun et al.*, 2016). This approach may create an issue especially towards high *T*, where highly concentrated suspension droplets are typically utilized to diagnose their freezing ability. High particle concentrations also promote particle aggregation and gravitational settling out of the droplet (*Beydoun et al.*, 2016; *Emersic et al.*, 2015).

In conclusion, our study indicates significant diversity between dry and aqueous suspension measurement techniques. The ratios of the individual measurements ($n_{s,ind}$) to the log average of $n_{s,geo}(T)$ range 0.6-1.4 across the examined *T* range. In general, the ratios of the log average of dry dispersion measurements are higher than those of aqueous suspension measurements. The observed discrepancy may be due to non-uniform active site density for different sizes and/or the alteration in physico-chemical properties of cellulose by liquid-suspending it. Unless otherwise defined, the cellulose system may not be an ideal calibrant at this moment. Given such a distinct difference between two subgroups of immersion freezing techniques, standardization of our methods, especially INP sampling and treatment, may be one approach to reduce the measurement diversity and valiability when we deal with a complex material like cellulose. A community-wide effort to identify specimen-specific limitations and characteristics of each technique, as well as consolidating the $n_{s,geo}(T)$ parameterization, is an alternative approach to achieve overall precise and accurate INP measurements.

References

Adachi, K., Sedlacek III, A. J., Kleinman, L., Chand, D., Hubbe, J. M., and Buseck, P. R.: Volume changes upon heating of aerosol particles from biomass burning using transmission electron microscopy, Aerosol Science and Technology, 1, 45–56, doi: https://doi.org/10.1080/02786826.2017.1373181, 2018.

5

Adachi, K., Chung, S. H., Friedrich, H., and Buseck, P. R.: Fractal parameters of individual soot particles determined using electron tomography: Implications for optical properties, J. Geophys. Res., 112, D14202, doi: 10.1029/2006JD008296, 2007.

10   Alexander, J. M., Bell, D. M., Imre, D., Kleiber, P. D., Grassian, V. H., and Zelenyuk, A.: Measurement of size-dependent dynamic shape factors of quartz particles in two flow regimes, Aerosol Science and Technology, 50, 870–879, doi: 10.1080/02786826.2016.1200006, 2016.

Archuleta, C. M., DeMott, P. J., and Kreidenweis, S. M.: Ice nucleation by surrogates for atmospheric mineral dust
15   and mineral dust/sulfate particles at cirrus temperatures, Atmos. Chem. Phys., 5, 2617-2634, doi: https://doi.org/10.5194/acp-5-2617-2005, 2005.

Atkinson, J. D., Murray, B. J., Woodhouse, M. T., Carslaw, K., Whale, T. F., Baustian, K., Dobbie, S., O'Sullivan, D., and Malkin, T. L.: The importance of feldspar for ice nucleation by mineral dust in mixed-phase clouds, Nature, 498,
20   355–358, doi:10.1038/nature12278, 2013.

Belosi, F., and Santachiara, G.: Ice-formation nuclei in Antarctica: new and past measurements
Atmos. Res., 145–146, 105–111, doi: https://doi.org/10.1016/j.atmosres.2014.03.030, 2014.

25   Benz, S., Megahed, K., Möhler, O., Saathoff, H., Wagner, R., and Schurath, U.: *T*-dependent rate measurements of homogeneous ice nucleation in cloud droplets using a large atmospheric simulation chamber, J. Photoch. Photobio. A, 176, 208–217, doi: https://doi.org/10.1016/j.jphotochem.2005.08.026, 2005.

Beranek, J., Imre, D., and Zelenyuk, A.: Real-time shape-based particle separation and detailed in situ particle shape
30   characterization. Analytical Chemistry, 84:1459-1465, doi: 10.1021/ac202235z, 2012.

Beydoun, H., Polen, M., and Sullivan, R. C.: Effect of particle surface area on ice active site densities retrieved from droplet freezing spectra, Atmos. Chem. Phys., 16, 13359–13378, doi: https://doi.org/10.5194/acp-16-13359-2016, 2016.

35

Bilde, M. and Svenningsson, B.: CCN activation of slightly soluble organics: the importance of small amounts of inorganic salt and particle phase, Tellus Series B – Chemical and Physical Meteorology, 56, 128–134, doi: https://doi.org/10.1111/j.1600-0889.2004.00090.x, 2004.

40   Brands, M., Kamphus, M., Böttger, T., Schneider, J., Drewnick, F., Roth, A., Curtius, J., Voigt, C., Borbon, A., Beekmann, M., Bourdon, A., Perrin, T., and Borrmann, S.: Characterization of a newly developed Aircraft-Based Laser Ablation Aerosol Mass Spectrometer (ALABAMA) and first field deployment in urban pollution plumes over Paris during MEGAPOLI 2009, Aerosol Sci. Technol., 45, 46–64, doi: https://doi.org/10.1080/02786826.2010.517813, 2011.

45

Budke, C. and Koop, T.: BINARY: an optical freezing array for assessing temperature and time dependence of heterogeneous ice nucleation, Atmos. Meas. Tech., 8, 689–703, doi: https://doi.org/10.5194/amt-8-689-2015, 2015.

50   Burkert-Kohn, M., Wex, H., Welti, A., Hartmann, S., Grawe, S., Hellner, L., Herenz, P., Atkinson, J. D., Stratmann, F., and Kanji, Z. A.: Leipzig Ice Nucleation chamber Comparison (LINC): intercomparison of four online ice nucleation counters, Atmos. Chem. Phys., 17, 11683–11705, doi: https://doi.org/10.5194/acp-17-11683-2017, 2017.

Clauss, T., Kiselev, A., Hartmann, S., Augustin, S., Pfeifer, S., Niedermeier, D., Wex, H., and Stratmann, F.: Application
55   of linear polarized light for the discrimination of frozen and liquid droplets in ice nucleation experiments, Atmos. Meas. Tech., 6, 1041–1052, doi: https://doi.org/10.5194/amt-6-1041-2013, 2013.

Cziczo, D. J., Stetzer, O., Worringen, A., Ebert, M., Weinbruch, S., Kamphus, M., Gallavardin, S. J., Curtius, J., Borrmann, S., Froyd, K. D., Mertes, S., Mohler, O., and Lohmann, U.: Inadvertent climate modification due to
60   anthropogenic lead, Nat. Geosci., 2, 333–336, doi: https://doi.org/10.1038/ngeo499, 2009.

DeMott, P. J., Prenni, A. J., McMeeking, G. R., Sullivan, R. C., Petters, M. D., Tobo, Y., Niemand, M., Möhler, O., Snider, J. R., Wang, Z., and Kreidenweis, S. M.: Integrating laboratory and field data to quantify the immersion freezing ice nucleation activity of mineral dust particles, Atmos. Chem. Phys., 15, 393–409, https://doi.org/10.5194/acp-15-393-2015, 2015.

5

Diehl, K., Quick, C., Matthias-Maser, S., Mitra, S. K., and Jaenicke, R.: The ice nucleating ability of pollen. Part I: Laboratory studies in deposition and condensation freezing modes, Atmos. Res., 58, 75–87, 2001.

Diehl, K., Debertshäuser, M., Eppers, O., Schmithüsen, H., Mitra, S.K., and Borrmann, S.: Particle-area dependence
10   of mineral dust in the immersion mode: investigations with freely suspended drops in an acoustic levitator. Atmos. Chem. Phys., 14, 12343–12355, doi: https://doi.org/10.5194/acp-14-12343-2014, 2014.

Emersic, C., Connolly, P. J., Boult, S., Campana, M., and Li, Z.: Investigating the discrepancy between wet-suspension- and dry-dispersion-derived ice nucleation efficiency of mineral particles, Atmos. Chem. Phys., 15,
15   11311–11326, doi: https://doi.org/10.5194/acp-15-11311-2015, 2015.

Fahey, D. W., Gao, R.-S., Möhler, O., Saathoff, H., Schiller, C., Ebert, V., Krämer, M., Peter, T., Amarouche, N., Avallone, L. M., Bauer, R., Bozóki, Z., Christensen, L. E., Davis, S. M., Durry, G., Dyroff, C., Herman, R. L., Hunsmann, S., Khaykin, S. M., Mackrodt, P., Meyer, J., Smith, J. B., Spelten, N., Troy, R. F., Vömel, H., Wagner, S., and Wienhold,
20   F. G.: The AquaVIT-1 intercomparison of atmospheric water vapor measurement techniques, Atmos. Meas. Tech., 7, 3177–3213, doi: https://doi.org/10.5194/amt-7-3177-2014, 2014.

Fornea, A.P., Brooks, S. D., Dooley, J. B., and Saha, A. Heterogeneous freezing of ice on atmospheric aerosols containing ash, soot, and soil, J. Geophys. Res., 114, D13201, doi: https://doi.org/10.1029/2009JD011958, 2009.

25

Garimella, S., Kristensen, T. B., Ignatius, K., Welti, A., Voigtländer, J., Kulkarni, G. R., Sagan, F., Kok, G. L., Dorsey, J., Nichman, L., Rothenberg, D. A., Rösch, M., Kirchgäßner, A. C. R., Ladkin, R., Wex, H., Wilson, T. W., Ladino, L. A., Abbatt, J. P. D., Stetzer, O., Lohmann, U., Stratmann, F., and Cziczo, D. J.: The SPectrometer for Ice Nuclei (SPIN): an instrument to investigate ice nucleation, Atmos. Meas. Tech., 9, 2781–2795, doi: https://doi.org/10.5194/amt-9-
30   2781-2016, 2016.

Garimella, S., Rothenberg, D. A., Wolf, M. J., David, R. O., Kanji, Z. A., Wang, C., Rösch, M., and Cziczo, D. J.: Uncertainty in counting ice nucleating particles with continuous flow diffusion chambers, Atmos. Chem. Phys., 17, 10855–10864, doi: https://doi.org/10.5194/acp-17-10855-2017, 2017.

35

Garimella, S., Rothenberg, D. A., Wolf, M. J., Wang, C., and Cziczo, D. J.: How uncertainty in field measurements of ice nucleating particles influences modeled cloud forcing, Journal of the Atmospheric Sciences, 75, 179–187, 2018.

Glen, A. and Brooks, S. D.: A new method for measuring optical scattering properties of atmospherically relevant
40   dusts using the Cloud and Aerosol Spectrometer with Polarization (CASPOL), Atmos. Chem. Phys., 13, 1345–1356, doi: 10.5194/acp-13-1345-2013, 2013.

Glen, A. and Brooks, S. D.: Single Particle Measurements of the Optical Properties of Small Ice Crystals and Heterogeneous Ice Nuclei, Aerosol Sci. Technol., 48, 1123–1132, doi: 10.1080/02786826.2014.963023, 2014.

45

Harrison, A. D., Whale, T. F., Rutledge, R., Lamb, S., Tarn, M. D., Porter, G. C. E., Adams, M., McQuaid, J. B., Morris, G. J., and Murray, B. J.: An instrument for quantifying heterogeneous ice nucleation in multiwell plates using infrared emissions to detect freezing, Atmos. Meas. Tech. Discuss., https://doi.org/10.5194/amt-2018-177, in review, 2018.

50

Hartmann, S., Niedermeier, D., Voigtländer, J., Clauss, T., Shaw, R. A., Wex, H., Kiselev, A., and Stratmann, F.: Homogeneous and heterogeneous ice nucleation at LACIS: operating principle and theoretical studies, Atmos. Chem. Phys., 11, 1753–1767, doi: https://doi.org/10.5194/acp-11-1753-2011, 2011.

55   Hiranuma, N., Hoffmann, N., Kiselev, A., Dreyer, A., Zhang, K., Kulkarni, G., Koop, T., and Möhler, O.: Influence of surface morphology on the immersion mode ice nucleation efficiency of hematite particles, Atmos. Chem. Phys., 14, 2315-2324, https://doi.org/10.5194/acp-14-2315-2014, 2014.

Hiranuma, N., Möhler, O., Yamashita, K., Tajiri, T., Saito, A., Kiselev, A., Hoffmann, N., Hoose, C., Jantsch, E., Koop,
60   T., and Murakami, M.: Ice nucleation by cellulose and its potential contribution to ice formation in clouds, Nat. Geosci., 8, 273–277, doi: https://doi.org/10.1038/ngeo2374, 2015a.

Hinz, K.-P., Greweling, M., Drews, F., and Spengler, B.: Data processing in on-line laser mass spectrometry of inorganic, organic, or biological airborne particles, Am. Soc. Mass Spectrom., 10, 648–660, doi: https://doi.org/10.1016/S1044-0305(99)00028-8, 1999.

5   Hoffmann, N., Duft, D., Kiselev, A., and Leisner, T.: Contact freezing efficiency of mineral dust aerosols studied in an electrodynamic balance: quantitative size and temperature dependence for illite particles, Faraday Discuss., 165, 383–390, doi:10.1039/C3FD00033H, 2013a.

Hoffmann, N., Kiselev, A., Rzesanke, D., Duft, D., and Leisner, T.: Experimental quantification of contact freezing in
10   an electrodynamic balance, Atmos. Meas. Tech., 6, 2373–2382, doi:10.5194/amt-6-2373-2013, 2013b.

Ickes, L., Welti, A., Hoose, C., and Lohmann, U.: Classical nucleation theory of homogeneous freezing of water: thermodynamic and kinetic parameters, Phys. Chem. Chem. Phys., 17, 5514–5537, doi: 10.1039/C4CP04184D, 2015.

15

Kiselev, A., Bachmann, F., Pedevilla, P., Cox, S. J., Michaelides, A., Gerthsen, D., and Leisner, T.: Active sites in heterogeneous ice nucleation—the example of K-rich feldspars, Science, 355, 367–371, doi: https://doi.org/10.1126/science.aai8034, 2017.

20   Knopf, D. A., Alpert, P. A., and Wang, B.: The role of organic aerosol in atmospheric ice nucleation: A review, ACS Earth Space Chem.*, 2*, 168–202, doi: 10.1021/acsearthspacechem.7b00120, 2018.

Koehler, K., Kreidenweis, S. M., DeMott, P. J., Petters, M. D., Prenni, A. J., and Carrico, C. M.: Hygroscopicity and cloud droplet activation of mineral dust aerosol, Geophys. Res. Lett. 2009, 36, L08805, doi: 10.1029/2009GL037348,
25   2009.

Koop, T. and Murray, B. J.: A physically constrained classical description of the homogeneous nucleation of ice in water, J. Chem. Phys., 145, 211915, doi: https://doi.org/10.1063/1.4962355, 2016.

30   Kumar, A., Marcolli, C., Luo, B., and Peter, T.: Ice nucleation activity of silicates and aluminosilicates in pure water and aqueous solutions – Part 1: The K-feldspar microcline, Atmos. Chem. Phys., 18, 7057–7079, https://doi.org/10.5194/acp-18-7057-2018, 2018.

Lakshmanan, C. M., Gal-or, B., and Hoelscher, H. E.: Production of levoglucosan by pyrolysis of carbohydrates,
35   *Product R&D*, *8*, 261–267, doi: 10.1021/i360031a010, 1969.

Lützenkirchen, J., Abdelmonem, A., Weerasooriya, R., Heberling, F., Metz, V., and Marsac, R.: Adsorption of dissolved aluminum on sapphire-c and kaolinite: implications for points of zero charge of clay minerals, Geochem. Trans., 15, 1-14, doi: 10.1186/1467-4866-15-9, 2014.

40

Madorsky, S. L., Hart, V. E., and Straus, S.: Pyrolysis of cellulose in a vacuum, Journal of Research of the National Bureau of Standards, 56, 343–354, 1956.

Marcolli, C.: Deposition nucleation viewed as homogeneous or immersion freezing in pores and cavities, Atmos.
45   Chem. Phys., 14, 2071–2104, doi: https://doi.org/10.5194/acp-14-2071-2014, 2014.

Marcolli, C.: Pre-activation of aerosol particles by ice preserved in pores. Atmos. Chem. Phys. 17, 1595–1622, 2017.

Miles, N. L., Verlinde, J., and Clothiaux, E. E.: Cloud droplet size distributions in low-level stratiform clouds, J. Atmos.
50   Sci., 57, 295–311, doi: https://doi.org/10.1175/1520-0469(2000)057<0295:CDSDIL>2.0.CO;2, 2000.

Möhler, O., Stetzer, O., Schaefers, S., Linke, C., Schnaiter, M., Tiede, R., Saathoff, H., Krämer, M., Mangold, A., Budz, P., Zink, P., Schreiner, J., Mauersberger, K., Haag, W., Kärcher, B., and Schurath, U.: Experimental investigation of homogeneous freezing of sulphuric acid particles in the aerosol chamber AIDA, Atmos. Chem. Phys., 3, 211–223,
55   doi: https://doi.org/10.5194/acp-3-211-2003, 2003.

Nicolet, M., Stetzer, O., Lüönd, F., Möhler, O., and Lohmann, U.: Single ice crystal measurements during nucleation experiments with the depolarization detector IODE, Atmos. Chem. Phys., 10, 313–325, doi: 10.5194/acp-10-313-2010, 2010.

60

Ohwoavworhua, F. O., and Adelakun, T. A.: Non-wood fibre production of microcrystalline cellulose from Sorghum caudatum: Characterisation and tableting properties. Indian Journal of Pharmaceutical Science, 72, 295–301, doi: 10.4103/0250-474X.70473, 2010.

O'Sullivan, D., Murray, B. J., Ross, J. F., Whale, T. F., Price, H. C., Atkinson, J. D., Umo, N. S., and Webb, M. E.: The relevance of nanoscale biological fragments for ice nucleation in clouds, Sci. Rep., 5, 8082, doi: 10.1038/srep08082, 2015.

5   Page, A. J. and Sear, R. P.: Heterogeneous nucleation in and out of pores, Phys. Rev. Lett., 97, 065701, doi: https://doi.org/10.1103/PhysRevLett.97.065701, 2006.

Peckhaus, A., A. Kiselev, T. Hiron, M. Ebert, and T. Leisner (2016), A comparative study of K-rich and Na/Ca-rich feldspar ice-nucleating particles in a nanoliter droplet freezing assay, *Atmos. Chem. Phys.*, *16*, 11477–11496, 10   doi:10.5194/acp-16-11477-2016.

Polen, M., Lawlis, E., and Sullivan, R. C.: The unstable ice nucleation properties of Snomax® bacterial particles, J. Geophys. Res., 121, 11666–11678, doi: 10.1002/2016JD025251., 2016.

15   Polen, M., Brubaker, T., Somers, J., and Sullivan, R. C.: Cleaning up our water: reducing interferences from nonhomogeneous freezing of "pure" water in droplet freezing assays of ice-nucleating particles, Atmos. Meas. Tech., 11, 5315–5334, https://doi.org/10.5194/amt-11-5315-2018, 2018.

Price, H. C., Baustian, K. J., McQuaid, J. B., Blyth, A., Bower, K. N., Choularton, T., Cotton, R. J., Cui, Z., Field, P. R., 20   Gallagher, M., Hawker, R., Merrington, A., Miltenberger, A., Neely, R. R., Parker, S. T., Rosenberg, P. D., Taylor, J. W., Trembath, J., Vergara-Temprado, J., Whale, T. F., Wilson, T. W., Young, G., and Murray, B.J.: Atmospheric ice-nucleating particles in the dusty tropical Atlantic. J. Geophys. Res. - Atmos., 123, 2175–2193, 2018.

Riechers, B., Wittbracht, F., Hütten, A., and Koop, T.: The homogeneous ice nucleation rate of water droplets 25   produced in a microfluidic device and the role of temperature uncertainty, Phys. Chem. Chem. Phys., 15, 5873–5887, doi: 10.1039/C3CP42437E, 2013.

Reicher, N., Segev, L., and Rudich, Y.: The Weizmann Supercooled Droplets Observation on a Microarray (WISDOM) and application for ambient dust, Atmos. Meas. Tech., 11, 233-248, doi: https://doi.org/10.5194/amt-11-233-2018, 30   2018.

Schill, G. P., Jathar, S. H., Kodros, J. K., Levin, E. J. T., Galang, A. M., Friedman, B., Link, M. F., Farmer, D. K., Pierce, J. R., Kreidenweis, S. M., and DeMott, P. J.: Ice-nucleating particle emissions from photochemically aged diesel and biodiesel exhaust, Geophys. Res. Lett., 43, 5524–5531, doi: https://doi.org/10.1002/2016GL069529, 2016.
35
Schwenker, R. F. and Beck, L. R.: Study of the pyrolytic decomposition of cellulose by gas chromatography, Journal of Polymer Science: Part C, 2, 331–340, doi: 10.1002/polc.5070020133, 1963.

Silva, P. J., Liu D.-Y., Noble, C. A., and Prather, K. A.: Size and chemical characterization of individual particles 40   resulting from biomass burning of local southern California species, *Environmental Science & Technology, 33*, 3068–3076, doi: 10.1021/es980544p, 1999.

Steinke, I., Möhler, O., Kiselev, A., Niemand, M., Saathoff, H., Schnaiter, M., Skrotzki, J., Hoose, C., and Leisner, T.: Ice nucleation properties of fine ash particles from the Eyjafjallajökull eruption in April 2010, Atmos. Chem. Phys., 45   11, 12945–12958, doi: https://doi.org/10.5194/acp-11-12945-2011, 2011.

Steinke, I.: Ice nucleation properties of mineral dusts, Thesis, University of Heidelberg/Karlsruhe Institute of Technology, December 4th, doi: 10.11588/heidok.00015967, 2013.

50   Stopelli, E., Conen, F., Zimmermann, L., Alewell, C., and Morris, C. E.: Freezing nucleation apparatus puts new slant on study of biological ice nucleators in precipitation, Atmos. Meas. Tech., 7, 129–134, doi: https://doi.org/10.5194/amt-7-129-2014, 2014.

Subramanyam, S. B., Kondrashov, V., Rühe, J., and Varanasi, K. K.: Low ice adhesion on nano-textured 55   superhydrophobic surfaces under supersaturated conditions, ACS Appl. Mater. Interfaces, 8, 12583–12587, doi: 10.1021/acsami.6b01133, 2016.

Sullivan, R. C., Moore, M. J. K., Petters, M. D., Kreidenweis, S. M., Qafoku, O., Laskin, A., Roberts, G. C. and Prather, K. A.: Impact of particle generation method on the apparent hygroscopicity of insoluble mineral particles, Aerosol 60   Sci. Technol., 44, 830–846, doi: 10.1080/02786826.2010.497514, 2010.

Tarn, M. D., Sikora, S. N. F., Porter, G. C. E., O'Sullivan, D., Adams, M., Whale, T. F., Harrison, A. D., Vergara-Temprado, J., Wilson, T. W., Shim, J. U., Murray, B. J.: The study of atmospheric ice-nucleating particles via microfluidically generated droplets, Microfluid Nanofluidics, 22, doi: 10.1007/s10404-018-2069-x, 2018.

Timko, M. T., Yu, Z., Kroll, J., Jayne, J. T., Worsnop, D. R., Miake-Lye, R. C., Onasch, T. B., Liscinsky, D., Kirchstetter, T. W., Destaillats, H., Holder, A. L., Smith, J. D., and Wilson, K. R.: Sampling artifacts from conductive silicone tubing, Aerosol. Sci. Tech., 43, 855–865, 2009.

5   Tobo, Y.: An improved approach for measuring immersion freezing in large droplets over a wide temperature range, Sci. Rep., 6, 32930, doi: 10.1038/srep32930, 2016.

Vali, G.: Quantitative evaluation of experimental results on the heterogeneous freezing nucleation of supercooled liquids, J. Atmos. Sci., 28, 402–409, doi: https://doi.org/10.1175/1520-0469(1971)028<0402:QEOERA>2.0.CO;2,
10   1971.

Vali, G.: Revisiting the differential freezing nucleus spectra derived from drop freezing experiments; methods of calculation, applications and confidence limits, Atmos. Meas. Tech. Discuss., https://doi.org/10.5194/amt-2018-309, in review, 2018.

15

Vochezer, P., Järvinen, E., Wagner, R., Kupiszewski, P., Leisner, T., and Schnaiter, M.: In situ characterization of mixed phase clouds using the Small Ice Detector and the Particle Phase Discriminator, Atmos. Meas. Tech., 9, 159–177, doi: 10.5194/amt-9-159-2016, 2016.

20   Wagner, R., Kiselev, A., Möhler, O., Saathoff, H., and Steinke, I.: Pre-activation of ice-nucleating particles by the pore condensation and freezing mechanism, Atmos. Chem. Phys., 16, 2025–2042, https://doi.org/10.5194/acp-16-2025-2016, 2016.

Wex, H., DeMott, P. J., Tobo, Y., Hartmann, S., Rösch, M., Clauss, T., Tomsche, L., Niedermeier, D., and Stratmann,
25   F.: Kaolinite particles as ice nuclei: learning from the use of different kaolinite samples and different coatings, Atmos. Chem. Phys., 14, 5529–5546, doi: https://doi.org/10.5194/acp-14-5529-2014, 2014.

Wex, H., Augustin-Bauditz, S., Boose, Y., Budke, C., Curtius, J., Diehl, K., Dreyer, A., Frank, F., Hartmann, S., Hiranuma, N., Jantsch, E., Kanji, Z. A., Kiselev, A., Koop, T., Möhler, O., Niedermeier, D., Nillius, B., Rösch, M., Rose,
30   D., Schmidt, C., Steinke, I., and Stratmann, F.: Intercomparing different devices for the investigation of ice nucleating particles using Snomax® as test substance, Atmos. Chem. Phys., 15, 1463–1485, doi: https://doi.org/10.5194/acp-15-1463-2015, 2015.

Whale, T. F., Murray, B. J., O'Sullivan, D., Wilson, T. W., Umo, N. S., Baustian, K. J., Atkinson, J. D., Workneh, D. A.,
35   and Morris, G. J.: A technique for quantifying heterogeneous ice nucleation in microlitre supercooled water droplets, Atmos. Meas. Tech., 8, 2437–2447, https://doi.org/10.5194/amt-8-2437-2015, 2015.

Whale, T. F., Holden, M. A., Wilson, T. W., O'Sullivan, D., and Murray, B. J.: The enhancement and suppression of immersion mode heterogeneous ice-nucleation by solutes, Chem. Sci., 9, 4142–4151, doi: 10.1039/C7SC05421A,
40   2018.

Wright, T. P. and Petters, M. D.: The role of time in heterogeneous freezing nucleation, J. Geophys. Res.-Atmos., 118, 3731–3743, doi: 10.1002/jgrd.50365, 2013.

45   Yu, Y., Alexander, M. L., Perraud, V., Bruns, E. A., Johnson, S. N., Ezell, M. J., and Finlayson-Pitts, B. J.: Contamination from electrically conductive silicone tubing during aerosol chemical analysis, Atmos. Environ., 43, 2836–2839, doi: https://doi.org/10.1016/j.atmosenv.2009.02.014, 2009.

Zelenyuk, A., Imre, D., Wilson, J., Zhang, Z., Wang, J., and Mueller, K.: Airborne single particle mass spectrometers
50   (SPLAT II & miniSPLAT) and new software for data visualization and analysis in a geo-spatial context, J. Am. Soc. Mass Spectrom., 26, 257–270, doi: 10.1007/s13361-014-1043-4, 2015.

Figures
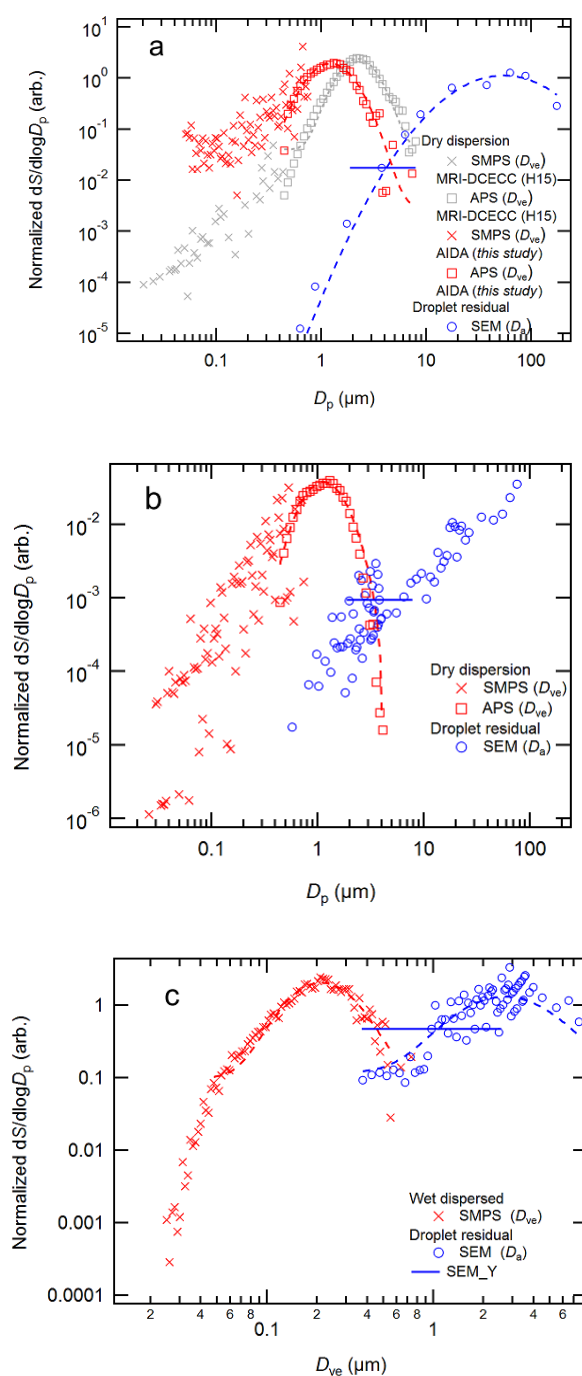
Figure S1. Surface area distributions of MCC (a), FC (b) and NCC (c) particles (red) and residuals (blue). Dry dispersed particle size distributions of MCC and FC as well as atomizer-dispersed NCC size distributions were measured by a combination of an SMPS (0.01 to 0.8 µm) and an APS (0.4 to 16 µm). The APS data of atomizer-dispersed NCC is not shown because the measured particle counts hovered around the minimum detection limit of an APS (0.001 cm^{-3}). Size distributions of droplet residuals of each particle type were measured using the off-line SEM analysis (as small as 0.3 µm). All data points represent the particle surface area distributions normalized to the total surface area concentration. The dashed lines on SMPS and APS data points represent the lognormal fits [i.e., $y_0 + A \exp(-1(\ln(x/\mu)/\sigma))$] for >85 nm D_{ve} and >0.5 µm D_{ve}, respectively. The x-axis error bar on a selected SEM data point reflects the range of uncertainty in the particle size derived from the average aspect ratio of each particle type (i.e., 2.05, 2.03 and 2.62 for MCC, FC and NCC, respectively, from an electron micrograph). Note that both axes are in the log scale.
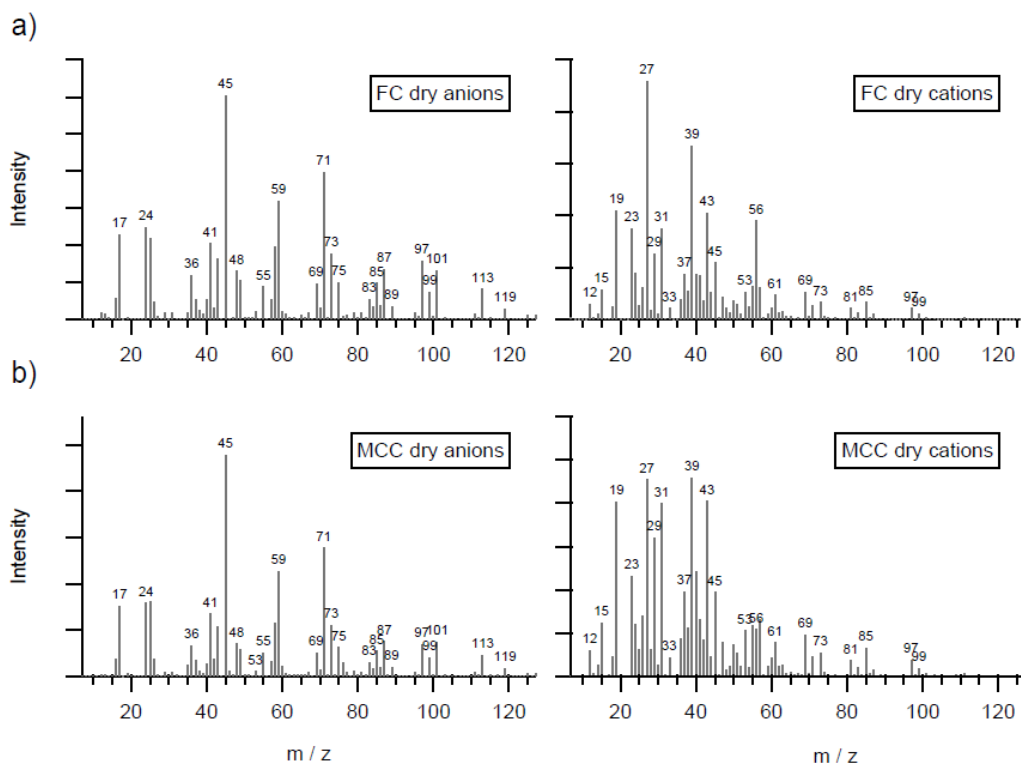
Figure S2. Laboratory reference mass spectra of dry dispersed cellulose particles with ALABAMA. a) Fibrous cellulose (FC), b) Microcrystalline cellulose (MCC), left: anions, right: cations. These mass spectra represent between 60 and 75% of the particles (FC: 1585 out of 2071; MCC: 193 out of 329).
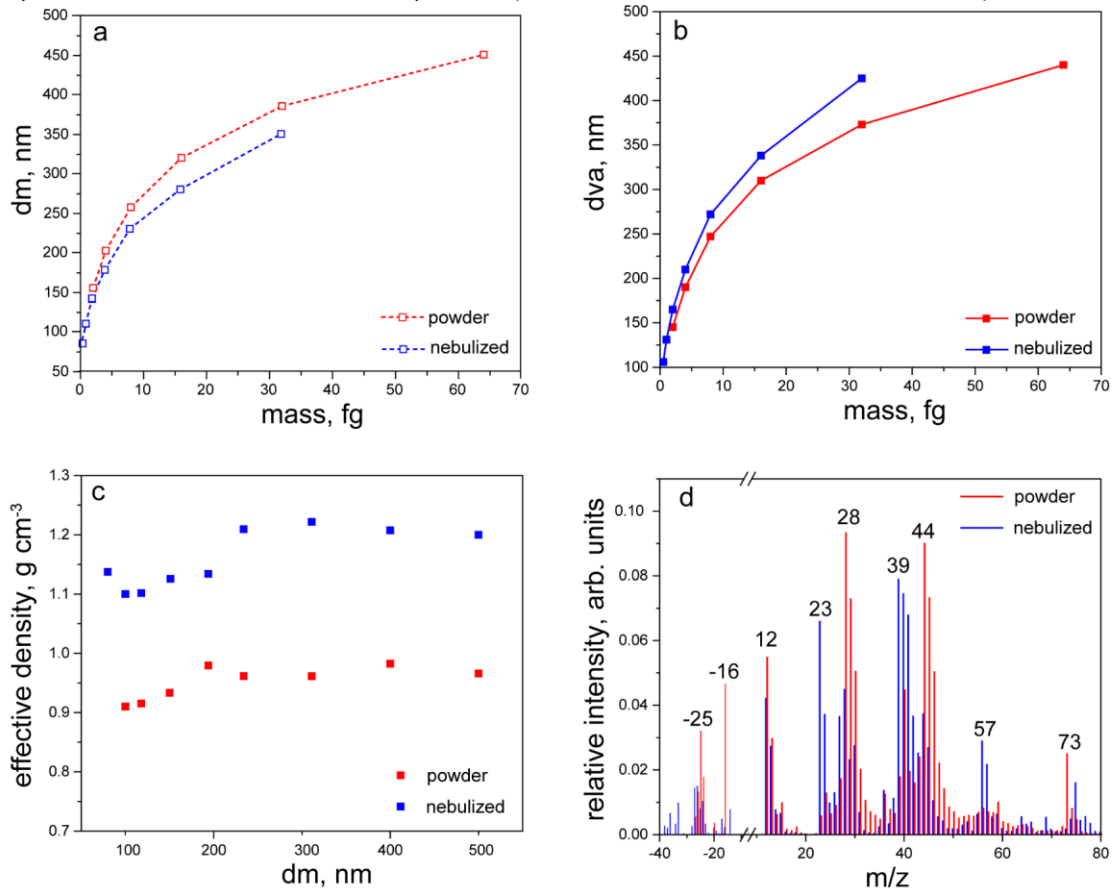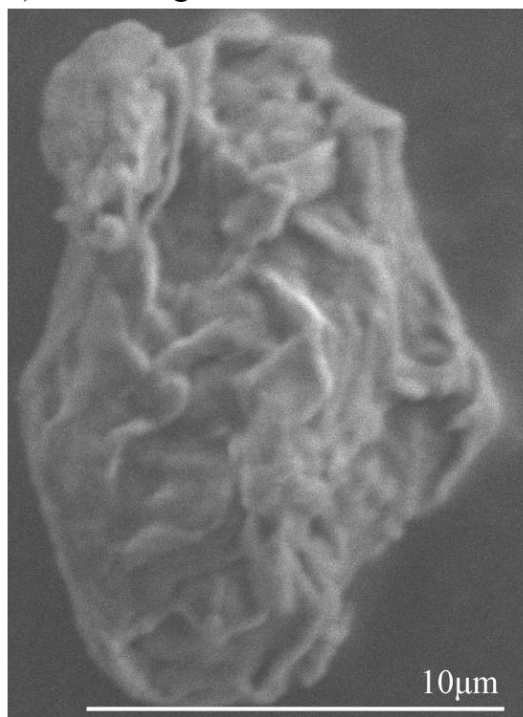

Figure S3. Aerosol particles mobility diameter (d_m) (a), vacuum aerodynamic diameter (d_{va}) (b), effective density (c) and mass spectra (d) of dry powder (red) and nebulized (blue) MCC particles.

a) SEM image

b) Line image
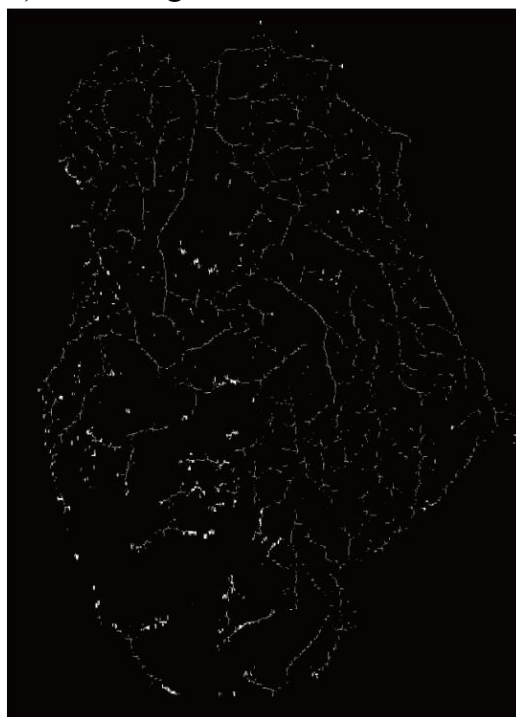
Figure S4. An example of surface image analysis. SEM image of a MCC particle (a) and its extracted surface line structure image analysed using an Interactive Data Language (IDL) program (b).
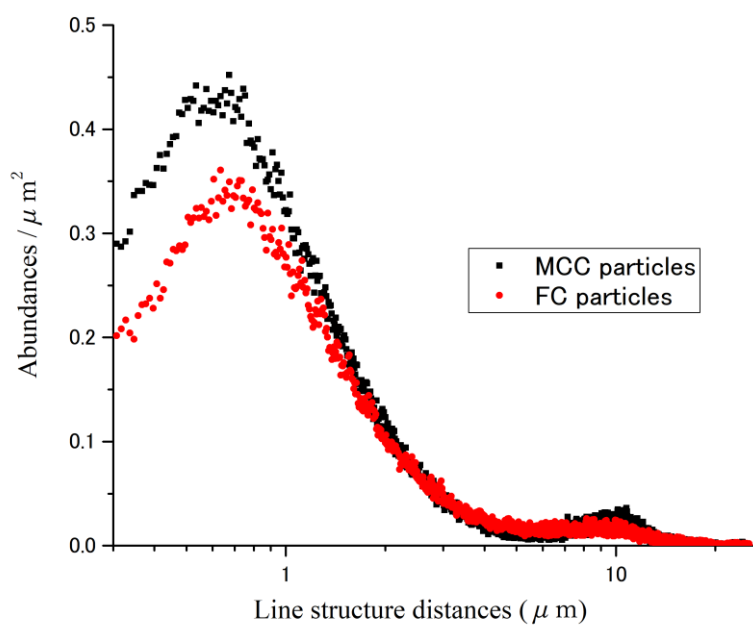
5

Figure S5. A compiled surface abundance of line structures scaled to the particle surface area as a function of line structure length for MCC and FC particles (61 MCC and 62 FC particles). An example of surface image analysis used for the plot is shown in **Fig. S4**. Peaks with smaller than 0.2 μm include noise and are excluded.

10

a) b) c) d) e) f)

➤ Carbon substrate ➤ NCC fibers ➤ Particulate aggregates of NCC fibers

Figure S6. TEM and SEM images of NCC samples. individual NCC fibers over a formvar carbon substrate (a). They form networks (white arrows) with some particulate aggregates (red arrows) (b and c). A stack of NCC fiber (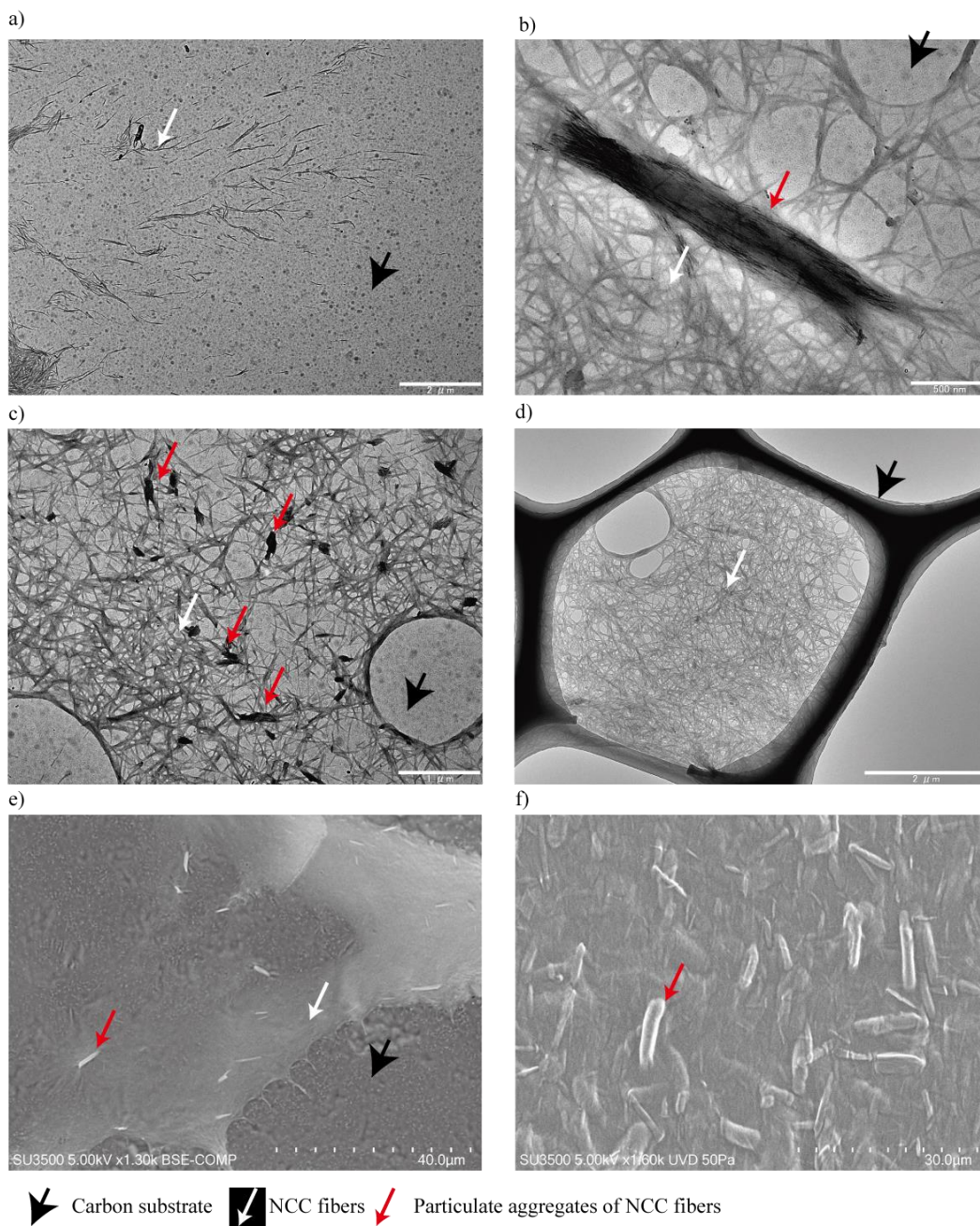white arrow) within a hole of lacey carbon substrate (black arrow) (d). SEM images of a layer with particulate NCC (red arrows) (e and f).

5

10
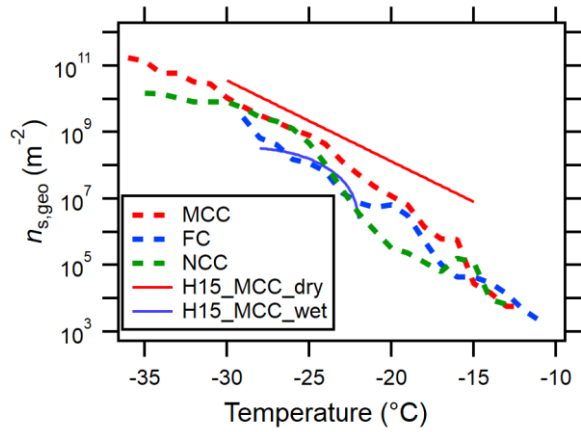
Figure S7. The *T*-binned log average of INAS density for MCC, FC, NCC. Reference immersion freezing $n_s(T)$ spectra are provided as in **Manuscript Fig. 3**.

5
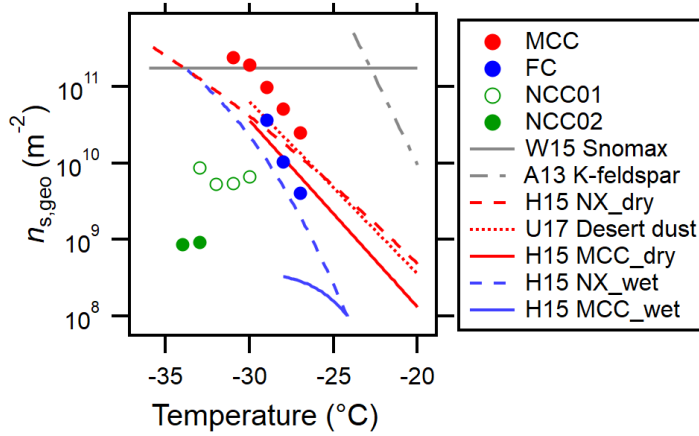
Figure S8. Derived INAS density for MCC, FC, NCC01 and NCC02. Reference immersion freezing $n_{s,geo}(T)$ spectra are provided as in **Manuscript Fig. 3**. Note that the uncertainties at each data point with respect to temperature and $n_{s,geo}(T)$ are ± 0.3 °C and ± 35%, respectively (**Table S1**).

10
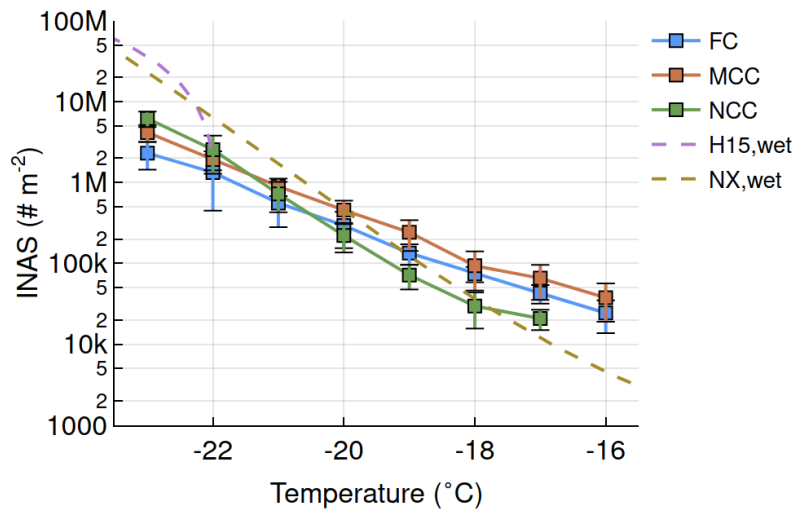
Figure S9. Derived INAS density for FC, MCC, NCC with parameterizations $n_{s,geo}^{H15MCC,wet}$ and $n_{s,geo}^{H15NX,wet}$ superimposed.
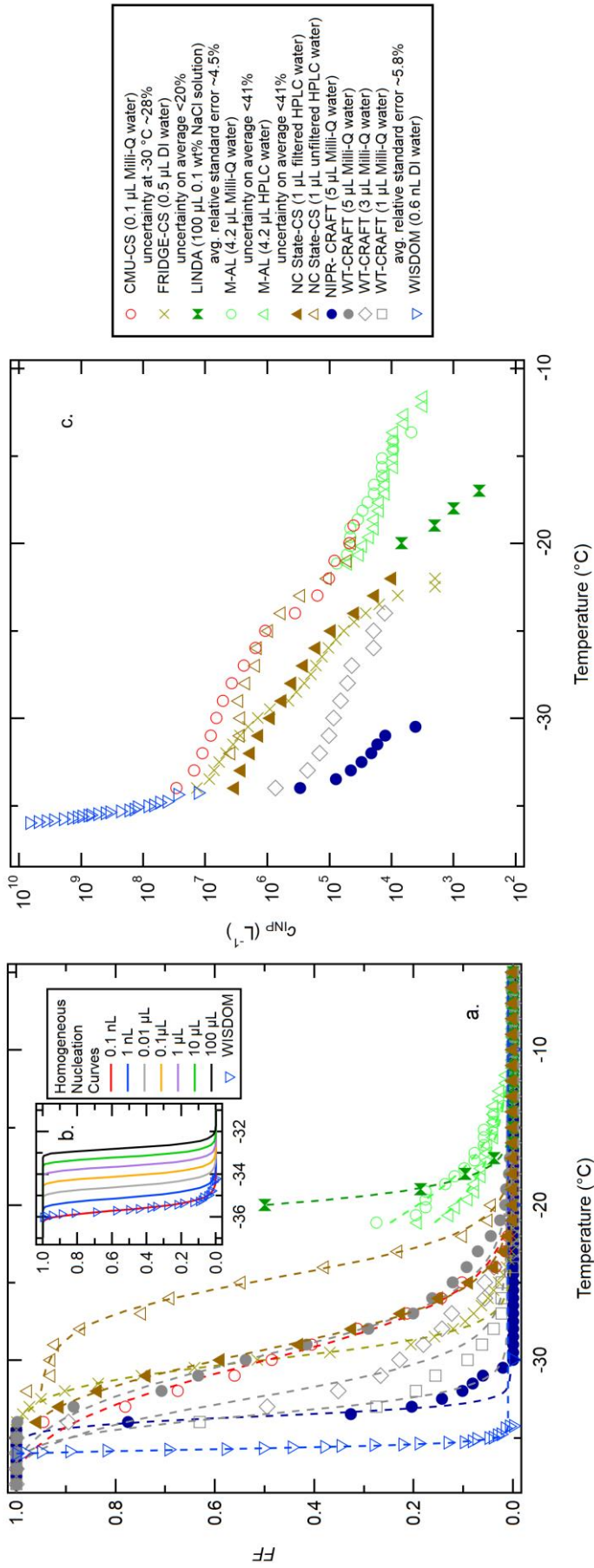
Figure S10. Freezing spectra of water samples of different purity used for aqueous suspension methods. Four freezing spectra with respect to measured frozen fraction, *FF* (a), homogeneous nucleation *FF* curves with a cooling rate of 1 °C min⁻¹ based on *Koop and Murray* (2016) (b) and INP per unit volume of water, c_{INP} (c) are shown as a function of temperature. Sigmoidal fits are also shown in (a). Relevant experimental uncertainties are also included in the figure legends. Conversion from *FF* to c_{INP} (vice versa) is prescribed in **Eqns. 3-4** In the main manuscript. Note that the cumulative frozen fraction (b) is estimated using the nucleation rate derived from a polynomial fit to the CNT based parameterization in Fig. 4 of *Koop and Murray* (2016).

Table S1. Quantitative method descriptions of dry dispersion techniques

ID	Instrument	Aerosol size	SSA (m² g⁻¹)[1]	Droplet size (volume)	Droplet number examined per experiment	Typical ratio of the MCC size to the droplet size	Cooling rate or ice nucleation time	Ice nucleation parametrization[2]	Uncertainties	Δlog($n_{s,geo}$)/ΔT for MCC)*	Solution wt% (if used)
1	AIDA	MCC and FC: polydisperse (mode ~1.2 μm) NCC: Polydisperse (mode ~200 nm)	MCC: 3.35, FC: 3.35, NCC: 18.59	9.38 μm on average (4.32 x 10⁻⁷ μL)	2.73 x 10⁹ to 7.19 x 10¹⁰ assuming full droplet activation in 84 m³ vessel	0.13	0.90 ± 0.2 °C min⁻¹, ³	Eqn. (1); AF using a combination of CPC, SMPS and APS for aerosol count	Temperature ± 0.3 °C (*Möhler et al.*, 2003), RH_w ± 5%, respectively (*Fahey et al.,* 2014), $n_{s,geo}(T)$ for immersion freezing of ± 35% (*Steinke et al.*, 2011)	0.24	NCC: 0.14[4]
2	CSU-CFDC	MCC: both polydisperse (mode at ~1.3 μm) and 500 nm (DMA 3081, TSI) FC: 500 nm (DMA 3081, TSI), NCC: 600 nm (DMA 3081, TSI)	MCC (poly): 2.09, MCC (500 nm): 8.00, FC (500 nm): 8.00, NCC (600 nm): 6.67	~2.6 μm (9.20 x 10⁻⁹ μL) for 0.5 μm dry particles at 5% SS_w and a CFDC temperature of -30 °C according to the model result; For a 1.5 micron dry particle, the droplet size for 105% RH is 3.0 microns (1.41 x 10⁻⁸ μL)	MCC and FC: 150,000; NCC: 1,500,000	0.19 (500 nm) - 0.40-0.50 (poly)	N/D (No Data)	Eqn. (1); AF using a combination of CPC, SMPS and APS for aerosol count	Temperature ± 0.5 °C, $n_{s,geo}(T)$ for immersion freezing of ± 60%, RH_w ± 1.6, 2 and 2.4% at -20, -25, and -30 °C, respectively	0.05 (500 nm) - 0.39 (poly)	NCC: 0.03
3	DFPC-ISAC	MCC and FC: polydisperse (mode ~300 nm)	MCC: 0.71-4.59 FC: 0.81-4.95 Values varied depending on the cyclone impactor cut-size[5]	N/D	~300-400 (examined crystals)	N/A (Deposition)	15 min	Eqn. (1); AF using a total aerosol count of OPC (> 0.3 μm diameter)	Temperature ± 0.1 °C, Saturation ratio, S_w at -22 °C of 1.02 ± 0.01, OPC error of ± 33%, The overall $n_{s,geo}(T)$ uncertainties of ~35%	0.24	MCC and FC: 0.1
4	EDB	MCC: 320 and 800 nm (DMA 3081, TSI)[6]	MCC (320 nm): 7.4 MCC (800 nm): 1.3	90 ± 5 μm (3.82 x 10⁻⁴ ± 6.54 x 10⁻⁸ μL)	100-200 (*Hoffmann et al.*, 2013a; 2013b)	0.0036-0.0089 (Contact)	<30 s	FF derived from the ratio of ice crystals to the total number of droplets[7]	Temperature ± 0.2 °C, $n_{s,geo}(T)$ for immersion freezing of ~two orders of magnitude (in part because of the aspherical shape of the particles)	0.38-0.44	N/A

ID	Instrument	Aerosol size	SSA (m^2 g^{-1})[1]	Droplet size (volume)	Droplet number examined per experiment	Typical ratio of the MCC size to the droplet size	Cooling rate or ice nucleation time	Ice nucleation parameterization[2]	Uncertainties	$\Delta\log(n_{s,geo})$/ΔT for MCC*	Solution wt% (if used)
5	FRIDGE-default	MCC: polydisperse (rather equally distributed from 300nm-5µm, no mode derivable)	MCC (dep.): 1.82[8] NCC: N/D (presumed to be same as AIDA)	No supercooled droplets are formed when FRIDGE works in a default mode.	No droplets (default mode), activated INPs: 100-1000[9]	N/A (Deposition)	100 s	Eqn. (1); AF is derived from the ratio of ice crystals on a wafer and total number of aerosols is estimated by an TSI OPS (0.3-10 µm diameter).	Temperature ± 0.2 °C, $n_{s,geo}(T)$ ± 40% at -20 °C, The $n_{s,geo}(T)$ error may become lower with decreasing temperature.	0.17	N/A
6	INKA	MCC: polydisperse (same as AIDA)	N/D (presumed to be same as AIDA)	N/D	Not Provided	N/D	~10 s	Eqn. (1); AF using a combination of CPC, SMPS and APS for aerosol count	Temperature ± 1.0 °C, S_w± 5%	0.14	N/A
7a	LACIS_dry	MCC: polydisperse (mode size 0.6 µm)	MCC (poly): 7.00	~5 µm (6.54 x 10^{-8} µL)	>2000	0.12	1.6 s (*Wex et al.*, 2014; *Hartmann* et al., 2011)	Eqn. (1); FF (full expression, not approximated)	Temperature ± 0.3 °C, The error in $n_{s,geo}(T)$ at -31 °C is ~25%	0.17	N/A
7b	LACIS_wet	MCC: 700 nm (DMA type Vienna Hauke medium)	MCC (700 nm): 5.70	~5 µm (6.54 x 10^{-8} µL)	>2000	0.14				0.05	MCC: 1.0
8	MRI-DCECC	MCC: polydisperse (mode diameter of ~2.2 µm,)	MCC (poly): 1.36	<30 µm (<1.41 x 10^{-5} µL)	4.66 x 10^8 to 1.92 x 10^9 (H15a) assuming full droplet activation in 1.4 m^3 vessel	0.35	2.4-2.8 °C min^{-1}	Eqn. (1); AF using a combination of CPC, SMPS and APS	Temperature ± 1.0 °C, 61% percent relative uncertainty in $n_{s,geo}(T)$ (*Hiranuma et al.*, 2015a)	0.17	N/A
9	PNNL-CIC	MCC: 600 nm (DMA 3081, TSI)	MCC (600 nm): 6.67	~5 µm (6.54 x 10^{-8} µL)	Not Provided	0.12	~12 s	Eqn. (1); AF based on the CPC aerosol count	Temperature ± 1.0 °C, RH_w ± 3%, The $n_{s,geo}(T)$ error is ~ ± one order of magnitude at any $n_{s,geo}(T)$ space.[10]	0.13	N/A

*The slope parameters of the other sample types for each technique are discussed in **Sect. 4.3.**, 1. Specific surface area, 2. Activated Fraction (*AF*) or Frozen Fraction (*FF*) - *AF* is calculated as the ratio of detected ice crystals to the number of total aerosol particles measured, whereas *FF* is derived from the ratio of ice crystals to the total particles detected in the subset of the sample (e.g., # of droplets) (*Burkert-Kohn et al.*,

2017). Our observation suggests that *AF*-based techniques appear to show higher $n_{s,geo}(T)$ than *FF*-based ones at $T > -16$ °C. This is opposite to the observation addressed in *Burkert-Kohn et al.* (2017), where two in-situ *FF* techniques (including LACIS) showed *FF* that were roughly a factor of 3 above the *AF* values determined from two CFDCs., A similar observation is addressed in *Burkert-Kohn et al.* (2017)., 3. Average ± standard error calculated using the data recorded every five seconds for 90-400 sec (0.65-1.11 °C min^{-1}), 4. ~3 mL of 3wt% NCC in 100 mL of Milli-Q H$_2$O, 5. Summarized in **Table 5** - relevant discussions are give in **Sect. 4.3.2.**, 6. Surface area has been calculated from SEM images of MCC particles collected on Nuclepore membrane filters., 7. *FF* was then converted into probability of freezing on a single collision (e_c) taking into account the rate of collision., 8. Measured with an OPS and corrected for a factor of 0.45, 9. The optimum number of INPs is 100-1000. The average number of cellulose particles per wafer was ~2x10^5., 10. Complete activation of water droplets was not observed; therefore, there may have been the chance of underestimating the INP concentration.

Table S2. Quantitative method descriptions of aqueous suspension techniques

ID	Instrument	Aerosol size	SSA (m² g⁻¹)[1]	Equivalent droplet size (volume)	Droplet or vial number examined per experiment	Typical ratio of the MCC size to the droplet size[2]	Cooling rate (°C min⁻¹)	IN parameterization[3]	Uncertainties	Δlog($n_{s,geo}$)/ΔT for MCC*	Solution wt%
10	BINARY	Bulk (Table 1)	MCC (bulk): 0.068 FC (bulk): 0.087 NCC (bulk): 1.24	1,046 µm (0.6 µL)	36 or 64	0.019 (0.001 wt%)	1.0	Eqns. (3)-(5); *FF*	Temperature ± 0.3 °C[4], $n_m(T)$ ± 20% based on Gaussian error calculation and 35% for the maximal error	0.38	All: 0.001 to 0.1
11	CMU-CS	Bulk (Table 1)	MCC (bulk): 0.068 FC (bulk): 0.087 NCC (bulk): 1.24	576 µm (0.1 µL)	30-40	0.009 (0.0001 wt%)	1.0	Eqns. (3)-(5); *FF*	Temperature ± 0.5 °C, *FF* uncertainties are on average 46, 57 and 75% for NCC, FC and MCC based on 95% confidence levels.	0.20	MCC: 0.0001, 0.01, 0.05 and 0.1; FC: 0.01, 0.1 and 1; NCC: 0.003, 0.03 and 0.1
12	FRIDGE-CS[5]	Bulk (Table 1) and polydisperse (no mode derivable)	MCC (poly): 1.71 NCC (bulk): 1.24	985 µm (0.5 µL)	~100[6]	0.0087 (0.0001 wt%)	1.0	Eqns. (3)-(5); *FF*	Temperature ± 0.2 °C, $n_{s,geo}(T)$ >20%[7]	0.31	MCC: 0.00010, 0.00020, 0.00043, FC: 0.00201, 0.00269, 0.02368, NCC: 0.049, 0.0049, 0.00049, 0.000049, 0.0000049
13	Leeds-µl-NIPI	Bulk (Table 1)	MCC (bulk): 0.068 FC (bulk): 0.087	1,241 µm (1 µL)	~40	0.0874 (0.1 wt%)	1.0	Eqns. (3)-(5); *FF*	Temperature ± 0.4 °C, Our $n_{s,geo}(T)$ error bars are calculated by propagating the uncertainties from droplet volume and weighing of the cellulose and water (*Whale et al.*, 2015).	0.47	MCC and FC: 0.1
14	LINDA	Bulk (Table 1)	MCC (bulk): 0.068 FC (bulk): 0.087 NCC (bulk): 1.24	Bulk solution (100 µL)	52	0.0874 (0.1 wt%)	0.4	Eqns. (3)-(5); *FF*	Temperature ± 0.2 °C, cumulated uncertainties (counts and temperature) of $n_{s,geo}(T)$ -48% to +64% for counts of 1 INA/mL, uncertainties of -36% to + 59% for counts of 10 INA/mL	0.29	All: 0.1[8]
15	M-AL	Bulk (Table 1)	MCC (bulk): 0.068 FC (bulk): 0.087 NCC (bulk): 1.24	1,900-2,100 µm (3.59-4.85 µL)	100	0.0874 (0.1 wt%)	N/A	Eqns. (3)-(5); *FF*	Temperature ± 0.7 °C, Our $n_{s,geo}(T)$ uncertainties for MCC, FC and NCC are on average 33%, 17% and 23%, respectively.[9]	0.40	MCC and FC: 0.1 and 1, NCC: 0.001, 0.01 and 0.1

ID	Instrument	Aerosol size	SSA (m^2 g^{-1})[1]	Equivalent droplet size (volume)	Droplet or vial number examined per experiment	Typical ratio of the MCC size to the droplet size[2]	Cooling rate (°C min^{-1})	IN parameterization[3]	Uncertainties	$\Delta\log(n_{s,geo})/\Delta T$ for MCC*	Solution wt%
16	M-WT	Bulk (Table 1)	MCC (bulk): 0.068 FC (bulk): 0.087	700 µm (0.18 µL)	50	0.0874 (0.1 wt%)	Isothermal	Eqns. (3)-(5); *FF*	Temperature ± 0.5 °C, The $n_{s,geo}(T)$ errors for MCC and FC are 26-48% and 32-53%, respectively.[10]	0.26	MCC and FC: 0.1
17	NC-State CS	Bulk (Table 1)	MCC (bulk): 0.068 FC (bulk): 0.087 NCC (bulk): 1.24	1,241 µm (1 µL)	64 (MCC and FC) 200 (NCC)	0.874 (1 wt%)	2.0	Eqns. (3)-(5); *FF*	Temperature ± 1 °C for MCC and FC, and ± 0.2 °C NCC, based on manufacturer specified thermistor accuracy. Uncertainties in INP concentration per unit liquid are derived based on one standard deviation of INP concentrations derived at each whole Kelvin across each experiment on the sample.[11]	0.29	MCC and FC: 1.0, NCC: 0.05
18	NIPR-CRAFT	Bulk (Table 1) and <10 µm[12]	MCC (bulk): 0.068 MCC (<10 µm): 3.35[13] FC (bulk): 0.087 FC (<10 µm): 3.35[13] NCC (bulk): 1.24	2,122 µm (5 µL)	49	0.0041-0.0188 (0.00001-0.001 wt%)	1.0	Eqns. (3)-(5); *FF*	Temperature ± 0.2 °C	0.41	All: 0.00001, 0.001 and 0.1
19	WISDOM	Bulk (Table 1)	MCC (bulk): 0.068 NCC (bulk): 1.24	34-96 µm (0.02-0.46 nL)	120-550	0.0693 (0.05 wt%)	1.0	Eqns. (3)-(5); *FF*	Temperature ± 0.3 °C, The error in $n_{s,geo}(T)$ of 16% is based on 95% confidence interval. Further uncertainty may arise from the BET surface area uncertainty (12%) and droplet volume identification (7%).	0.26	MCC: 0.05, NCC, 1.00-1.33
20	WT-CRAFT	Bulk (Table 1)	MCC (bulk): 0.068 FC (bulk): 0.087	1,789 µm (3 µL)	49	0.0322 (0.005 wt%)	1.0	Eqns. (3)-(5); *FF*	Temperature ± 0.5. The c_{INP} and n_m uncertainties are ±23.5% based on the relative standard error of three measurements of 0.05 wt% FC (sonicated samples).	0.36	MCC and FC: 0.05 and 0.005

*The slope parameters of the other sample types for each technique are discussed in **Sect. 4.3.**, 1. Specific surface area, 2. The aerosol size is based on the mass equivalent aerosol diameter for the given weight percent, at which ice nucleation ability of MCC was evaluated for <-20 °C. This temperature range is directly comparable to the dry dispersion measurements., 3. Activated Fraction (*AF*) or Frozen Fraction (*FF*) - *AF* is calculated as the ratio of detected ice crystals to the number of total aerosol particles measured, whereas *FF* is derived from the ratio of ice crystals to the total particles detected in the subset of the sample (e.g., # of droplets) (*Burkert-Kohn et al*., 2017). Our observation suggests that *AF*-based techniques appear to show higher $n_{s,geo}(T)$ than *FF*-based ones at T >-16 °C. This is opposite to the observation addressed in *Burkert-Kohn et al*. (2017), where two in-situ *FF* techniques (including LACIS) showed *FF* that were roughly a factor of 3 above the *AF* values determined from two CFDCs., 4. See *Budke and Koop*

(2015) for more details., 5. The dew point maintained to avoid evaporation/condensation while measuring. Note that we utilized aerosolized particles collected on filters and scrubbed with deionized water. The measured geometric *SSA* of dispersed MCC was 1.71 $m^2\,g^{-1}$, 6. We typically carry out a set of >four runs with >~100 droplets per run., 7. Higher $n_{s,geo}(T)$ uncertainties may coincide with the high temperature quartile because the span of the confidence interval is relatively wider when there exists only few frozen droplets., 8. Suspension was prepared in two different ways for MC and FC. 1) solution of 0.1 wt% sonicated and vortexed, 2) powder in the vials and addition of NaCl 0.1 wt% solution to the desired final weight percent cellulose of 0.1 wt%. NCC prepared as 1). Cellulose fibers tend to sediment and form clumps in solution., 9. The $c_{INPs}(T)$ and $n_{s,geo}(T)$ uncertainties were calculated taking the errors of the frozen fractions of drops, the specific particle surface area, the particle masses per drop, and the drop sizes into account., 10. The c_{INPs} and n_s uncertainties include errors of the frozen fractions of drops, the specific particle surface area, the particle masses per drop and the drop sizes., 11. For each sample multiple experiments were performed. An experiment consists of working with the same stock sample, and placing n droplets on the cold stage, cooling the stage. For the next experiment a new set of slides and droplets are prepared (MCC – 3 experiments ~64 drops/experiment; FC – 4 experiments ~64 drops/experiment; NCC – 3 experiments - ~200 drops/experiment; Filtered Water – 3 experiments ~200 drops/experiment; Unfiltered Water – 7 experiments ~64 drops/experiment). Individual INP spectra are binned to produce INAS concentrations in 1 K intervals. Reported INP spectrum's concentrations were produced by averaging the INAS concentration across each individual spectra. Note that droplets were placed on a hydrophobic glass slide and in contact with N_2. Oil immersion was not used., 12. Experiments with size-selected (<10 µm) particles, 13. The AIDA-derived geometric *SSA* value (3.35 $m^2\,g^{-1}$) is used since it accounts for only <10 µm particles.

Table S3. Nominal method descriptions of dry dispersion techniques

ID	Instrument	Dispersion method	Impactor type	Background correction method (if any)	Ice detection method	Valid data range	Sample pre-treatment	Solvent type (if used)
1	AIDA	MCC and FC: Rotating Brush (RBG1000, PALAS), NCC: modified atomizer[1]	Cyclone (D_{50} of 5 μm) combined with Rotating Brush	Background was neglected and no corrections was applied.[2]	Ice number counting per unit volume of air with optical particle counters (WELAS 2300 and 2500, PALAS, *Benz et al.*, 2005)	For MCC and FC, to exclude any possible artifacts from the chamber operation (e.g., sparse ice peak detection during abrupt cooling at the beginning), we examined data for 90-400 sec after the initial cooling and 1 min averaged *AF* >0.5% (INUIT06_07 for MCC, INUIT06_14 for FC). For NCC, we examined data for 90-400 sec after the initial cooling and welas count ~>0.1 p cm^{-3} (CIRRUS01_58).	Grinding MCC/FC with a mortar and pestle, Sonicating NCC for 30 min prior to the injection	Milli-Q water for NCC
2	CSU-CFDC	MCC and FC: Flask in a sonic bath and blowing dry N$_2$ over the sample, NCC: Medical nebulizer	Inertial impactor (cut-size of 2.4 μm)	Background INP concentrations calculated by taking measurements through a filter for 2-3 minutes before and after the sample period were accounted.[3]	Ice number counting per unit volume of air with an optical particle counter (OPC; CLiMET, model CI-3100)	This CFDC provided data for condensation/immersion freezing at -21.2, -25.1 and -29.7 °C (a total of eight data points with two, two and four points at around each temperature, respectively), which extended to a warmer region than the AIDA measurements. As demonstrated in *DeMott et al.* (2015), higher RH$_w$ values (105%) are required for full expression of immersion freezing in CSU-CFDC.	N/A	DI water for NCC
3	DFPC-ISAC	MCC(dry): Custom-built flask dust generator[4], MCC(wet): Nubulizer (AGK 2000, PALAS)	Cyclone (D_{50} of 7, 1 and 0.5 μm at 2, 12 and 3.5 lpm, respectively)	Background INP concentrations obtained by using blank filters (filters taken from the batch and processed into the DFPC chamber) were accounted.[5]	Visual inspection of individual freezing events based on an USB optical microscope (eScope) imagery and later inspected with ImageJ[6]	N/A	The suspensions were hand shaken before nebulization. A magnetic stirrer was used to keep the cellulose particles suspended.	MilliQ water for MCC and FC
4	EDB	Turbulent flow disperser[7]	Cyclone (D_{50} of 1 μm)	N/A	Visual inspection of individual freezing events according to the enhancement of scattered light on the linear CCD array upon freezing (*Hoffmann et al.*, 2013a)	N/A	N/A	Milli-Q water for MCC

ID	Instrument	Dispersion method	Impactor type	Background correction method (if any)	Ice detection method	Valid data range	Sample pre-treatment	Solvent type (if used)
5	FRIDGE-default	Mixing powder samples with a magnetic stirrer[8]	47 mm hydrophobic Fluoropore PTFE membrane with a 0.45 µm pore size bonded to a high-density polyethylene support produced by Merckmillipore®	The absolute number of ice crystals of a blank wafer was subtracted from the absolute number of ice crystals on a loaded wafer.[9]	Visual inspection of individual freezing events based on the CCD camera imagery of growing ice crystals	N/A	N/A	N/A
6	INKA	Rotating Brush (RBG1000, PALAS)	Cyclone (D_{50} of 5 µm) combined with Rotating Brush	An experiment started with a 2 minutes background measurement while sampling through a particle filter.[10]	Ice number counting per unit volume of air with an optical particle counter (OPC; CLiMET, model CI-3100)	This CFDC provided data for condensation and/or immersion freezing at around -25, -27.5, -30 and –30.5 °C (a total of eight data points with two, two, three and one point at around each temperature, respectively). Since INKA is of the same operational design as the CSU-CFDC, here also higher RH_w values (107%) were required for full expression of immersion freezing (*DeMott et al.*, 2015).	N/A	N/A
7a	LACIS_dry	Flask with an electric motor and blowing particle-free pressurized air input over the sample	Cyclone (D_{50} of 625 nm at 3 lpm)	N/A[11]	Ice number counting per unit volume of air according to the custom-built optical particle spectrometer, called TOPS-Ice (Thermo-stabilized Optical Particle Spectrometer for the detection of Ice; *Clauss et al.*, 2013)	N/A	N/A	N/A
7b	LACIS_wet	Modified atomizer[1]	N/A			N/A	We sonicated the sample for 10 minutes. The cumulative time required to obtain a sufficiently high number concentration at 700 nm was a week.[12, 13]	MilliQ water for MCC

ID	Instrument	Dispersion method	Impactor type	Background correction method (if any)	Ice detection method	Valid data range	Sample pre-treatment	Solvent type (if used)
8	MRI-DCECC	Rotating Brush (RBG1000, PALAS)	Cyclone (D_{50} of 2.5 µm and 1.0 µm)	No corrections were applied. Prior to experiments, a blank expansion was carried out to confirm the background non-IN active particle concentration of <0.1 cm^{-3}.	Ice number counting per unit volume of air with optical particle counters (WELAS Promo2000H, PALAS, *Benz et al.*, 2005)	N/A	N/A	N/A
9	PNNL-CIC	SSPD (Model 343, TSI)	N/A	Background INP concentrations calculated by taking measurements through a filter for 5 minutes before and after the sample period were accounted.[14]	Ice number counting per unit volume of air with an optical particle counter (OPC; CLiMET, model CI-3100).	$0.01 < AF < 0.95$ - Below 0.01 fraction, sensitivity of the instrument became an issue and was dependent upon particle concentration. Upper limit was governed by the particle losses in the system.	N/A	N/A

1. Similar to the commercially available atomizer (TSI 3076) drilled through an opposite orifice (*Wex et al*., 2015), 2. A blank reference expansion (*Hiranuma et al*., 2014) was carried out prior to a series of experiments to achieve the background non-IN active particle concentration in the chamber of <0.3 cm^{-3}., 3. A weighted average of the background INP concentration is calculated from the two filter periods and is subtracted from the average INP concentration of the sample period (*Schill et al*., 2016)., 4. Flow rate of ~12 lpm was employed. Cyclones (SCC, BGI, Inc.) were deployed downstream of the flask to exclude particles larger than certain aerodynamic diameter with varied cut-sizes (**Table 5**)., 5. In order to measure water background, we nebulized pure Milli-Q grade water onto Millipore filters and examined residuals to make sure no presence of water impurity. The filters were then processed with our DFPC chamber at -22 °C. The averaged crystal number on filter of seven was subtracted from the crystal number measured using cellulose samples (typically the order of two hundreds)., 6. N_{ice} is estimated by ImageJ software, followed by the Poisson statistic., 7. A flask containing cellulose and bronze beads is mixed with a magnetic stirrer and a synthetic air flow of 1 lpm., 8. Dry dispersion of cellulose into purified compressed air produced an aerosol concentration of approx. 10 cm^{-3} (MCC) and 40 cm^{-3} (FC)., 9. Background and particle losses (i.e., sampling efficiency, 90% of the surface of the wafer are analyzed) were accounted in our background corrections. Sampling volume was adjusted to avoid overloading of the wafers, water vapor depletion and merging of ice crystals before they were counted. So, the volume effect was neglected., 10. This procedure allowed to determine the background INPs caused by the chamber itself, which was then considered in the data analysis. In addition, particle losses in the sampling line were found to be negligible., 11. We did not observe any contribution from impurities in the water. For the detection of the homogeneous freezing limit, we used ammonium sulfate (dissolved in MilliQ water and sprayed with an atomizer) as seed particles for the droplets. We detected the first freezing of those highly diluted droplets at -38 °C. Hence, there was no need to correct the cellulose suspension data concerning the water background. We note that the experiment was stopped as soon as background originating from the ice covered walls was detected., 12. Swelling might have been an issue in the case of the suspension particles, because the sample needed to be prepared one week in advance. A 700 nm suspension particle was not necessarily comparable (in terms of chemical composition, morphology) to a 700 nm dry dispersed particle, but we did not investigate this further., 13. We found that the maximum of the size distribution depends on the suspension time of the cellulose particles. We measured size distributions directly after preparing the suspension, after one week and after two weeks, and observed size distribution broadening as well as a shift in mean diameter towards larger end., 14. A weighted average of the background INP concentration was calculated from the two filter periods and was subtracted from the average INP concentration of the sample period.

Table S4. Nominal method descriptions of aqueous suspension techniques

ID	Instrument	Solvent type	Sample pre-treatment	Suspension Descriptuion[1]	Background correction method	Ice detection method	Valid data range
10	BINARY	Bidistilled water	MCC and FC: described in *Hiranuma et al*. (2015a), NCC: one min ultrasonic bath and at least 10 min stirring with a vortex shaker after dilution of a weighed sample until pipetting; storage at +3 °C	Continuous stirring	No additional correction applied.	CCD camera: the digital images obtained by a CCD camera (QImaging MicroPublisher 5.0 RTV) were analyzed at a frequency that depends upon the experimental cooling rate (*Budke and Koop*, 2015).[2]	*FF* 0.05-0.95[3]
11	CMU-CS	Milli-Q water	MCC and FC: left unrefrigerated; suspended and stirred with no further processing, NCC: left refrigerated until using the sample; followed the protocol given by INUIT	All suspensions were continually stirred while pipetting. Constant stirring was done with a teflon stirbar while droplets were pipetted.	Cutoff *T* for background freezing was below -26 °C for these samples. All samples provided were given with the assumption that less than 10% of the *FF* would be attributable to water contamination.	Digital camera: The droplets were illuminated using a light-emitting diode light ring above the acrylic window, and the droplets were imaged using a stereomicroscope and digital camera (Amscope, *Polen et al*., 2016).[4]	MCC and FC: *FF* 0.05-0.95[3], NCC: *FF* >0.05[5]
12	FRIDGE-CS (immersion)	DI water	No pre-treatment applied	The suspension tube was shaken every ~20 sec to achieve a homogeneous distribution of cellulose particles in all droplets.[6]	The frozen fraction of DI water was subtracted from that of the suspension samples.[7]	CCD camera: a CCD camera (2/3" CCD > 5 megapixels, 1 pixel ~ 400 μm^2) was used to monitor and record the sample substrates.[8]	All range after the background correction
13	Leeds-μl-NIPI	Milli-Q water	Suspensions were stirred using a magnetic stirrer bar for approximately 30 min prior to pipetting out droplets. We did not sonicate suspensions.	Suspensions were continuously stirred during droplet preparation.	We used the freezing background and subtraction method described in *O'Sullivan et al*. (2015; i.e., Eqn. 1 and 2).[9]	Digital camera: The freezing of the droplets was monitored using a digital camera at a rate of one frame per sec. The first change in droplet structure (i.e., Fig. 2 of *Whale et al*., 2015) leading to droplet freezing was taken to be the nucleation event, and this information was used to establish the fraction of droplets frozen as a function of *T*.	All range after the background correction
14	LINDA	0.1 wt% NaCl solution	MCC and FC (Sus): 5 min sonication of suspension; manual shaking while pouring aliquots into vials, MCC and FC (Pow): 5 min sonication of grid with vials prior to analysis, NCC01: additional preliminary 15 min sonication of 3 wt% stock solution	Idle	No solvent vials froze until -18 °C. Therefore, no correction was applied.	CMOS camera: Images taken by a USB CMOS Monochrome Camera (DMK 72BUC02, The Imaging Source Europe GmbH, Bremen, Germany) were recorded every six sec (*Stopelli et al*., 2014).[10]	All range after the background correction

ID	Instrument	Solvent type	Sample pre-treatment	Suspension Description[1]	Background correction method	Ice detection method	Valid data range
15	M-AL	CHROMASOLV water for HPLC (Sigma-Aldrich)	No pre-treatment applied	Idle[11]	The frozen fraction of HPLC water was subtracted from that of the suspension samples.	Digital camera and infrared thermometer: the drops were imaged by a digital video camera and the surface temperature of the drops were measured directly by an infrared thermometer with a temporal resolution of 0.5 sec (*Diehl et al.*, 2014).[12]	*FF* 0.05-0.98[3]
16	M-WT	CHROMASOLV water for HPLC (Sigma-Aldrich)	No pre-treatment applied	Continuously stirring the suspension at a very low rate[13]	Since no freezing of HPLC water droplets was observed within the investigated temperature range, no background correction was applied.[14]	Visual observation during levitation[15]	*FF* 0.05-0.95[3, 16]
17	NC-State CS	HPLC Grade water (Aldrich)	All solutions were sonicated for 10 min prior to experimenting on the cold stage.	Idle	Background subtraction or correction was not applied in this study because median freezing temperatures for cellulose occurred several °C warmer than that of reference HPLC water.	Microscope camera: The droplets were imaged with a regular camera lens that was outfitted with a 2592 x 1944 pixel resolution camera (Infinity 1-5C; Lumenera, *Wright and Petters*, 2013).[17]	Temperature bins with ≥ 2 freeze events across all repeats (*n* = 3-7)
18	NIPR-CRAFT	Milli-Q water	No pre-treatment applied	Occasionally shaking a suspension tube while pipetting/preparing droplets	No ice nucleation of water was observed until ~-30°C. Therefore, no correction was applied.	Webcamera: individual droplet freezing events were monitored and recorded by a commercially available WEB camera (*Tobo*, 2016).[18]	MCC and FC: *FF* > 0.04[5], NCC: *FF* > 0.02-0.96[3]
19	WISDOM	Deionized water, biological grade	MCC: after sonication was applied, 30 min idle before droplets generation following the INUIT protocol, NCC: three cycles of sonication (by Hielscher vial-tweeter), 30 sec each, with 10 sec idle between	Idle (the time required to generate droplets was 30 sec)	Since all suspension droplets froze prior to the solvent's freezing, no correction was made.	Microscope camera: freezing experiments were observed under a light microscope (Olympus BX-51, 10X magnification, transmission mode) and a video file was recorded during the measurement with a temporal resolution of 1 sec (or temperature resolution of 0.017C for 1CPM cooling rate, *Reichar et al.*, 2018).[19]	All range after the background correction
20	WT-CRAFT	Milli-Q water	MCC and FC: sonication of 50 mL suspension in a falcon tube for 15 min	Idle	No correction was made.[20]	Webcamera (same as NIPR-CRAFT): manual counting of cumulative number of frozen droplets based on the color contrast shift in the off-the-shelf Webcamera (all videos recorded)[21]	*FF* > 0.05[5]; *T* > -26 °C (<3% pure water activation)

1. Description of the suspension solution while generating droplets/vial, 2. Three successive images were analyzed per 0.1K temperature interval, i.e., one image every 0.03K. Ice nucleation was determined optically based on the change in droplet brightness when the initially transparent liquid droplets became opaque upon freezing. This change in brightness was maximized by illuminating the droplets by LEDs at a low sideway angle from the top and also by the reflective top surface of the Peltier stage., 3. The FF range was restricted thereby limiting the valid data range, as a non-homogeneous particle distributions in bulk solution was presumed and, therefore, individual droplets leading to sparse nucleation at both low and high temperature boundaries are excluded. In order to exclude the effects of "pure" water freezing data beyond FF of 0.95 and higher was eliminated (this is an alternative to a water background subtraction). The impact of this correction was small as the resulting $n_{s,geo}(T)$ difference was within a factor of two., 4. Images were taken at a resolution of 1600×1200 with magnification of 7.5X at 0.17 °C intervals. Arrays containing between 30 and 40 droplets could be visualized. An image was recorded every 10s.

Images were analyzed manually to determine the temperature at which a liquid droplet (appearing gray) had frozen (appearing black)., 5. to exclude early freezers often represent the contaminant interference, 6. Aerosol was generated by dry dispersion of MCC particles. The particle number size distribution of this aerosol in the 0.3-10 μm diameter range was measured by an optical particle counter (3330, TSI). MCC particles were collected by filtration of the aerosol using cellulose nitrate membrane filters (Millipore, HABP04700). After sampling, the filters were placed in vials with 10 mL of deionized water. Particles were scrubbed from the filters by agitating for 10 min in an ultrasonic bath., 7. The background freezing contributed to <3% at -25 °C, <10% at -27.5°C and <20% at -29 °C. No evaporation/condensation was assumed., 8. LabView software was used to download images and detect changes in brightness of droplets (by comparing real time images with a reference image taken prior to the ice nucleation)., 9. To correct for the impact of background freezing on our data, we subtracted the $K(T)$ values for a best fit to the background freezing curve from the $K(T)$ values for the ice nucleation data. Where the data overlaps with the 68% confidence interval for the background freezing points were considered indistinguishable from the background and are not included. The cellulose data did not significantly overlap our background freezing., 10. LED array illuminated polycarbonate plate holding 52 sample tubes from the bottom. Light intensity in the area of each tube lid was extracted from each image and recorded into a text file together with the temperature at the time the image was taken., 11. Before refilling the medical syringe used for injecting droplets into M-AL, the suspension was stirred for approx. 20 sec. Before injecting, the syringe was shaken in order to homogenize the cellulose distribution in droplets., 12. The video camera allowed for the visual observation of the freezing process. The infrared thermometer was used to measure the surface temperature of the freezing drops with an accuracy of 0.7 K, while a Pt100 sensor was located in the vicinity of the drop to measure the ambient temperature. The freezing was detected as a sudden increase of the surface temperature to 0 °C., 13. Before the droplet injection, the syringe was shaken in order to homogenize the cellulose distribution in droplets., 14. Before each experiment, we carried out background test measurements, i.e. measurements with pure water droplets. The pure water drops were levitated in the tunnel for <35 s to minimize the effect of evaporation., 15. The experimenter observed the behavior of the levitating droplet; when the droplet freezes, it becomes opaque and its floating behavior changes abruptly., 16. Every single droplet was kept floating in the vertical air stream of the M-WT until it froze (within <35 sec). Freezing event within the first five seconds after injecting were presumably emanated from freezing triggered by contaminants and abandoned from our analysis. Conceptually, ~five sec is needed for a droplet to adapt its surface temperature to the ambient temperature., 17. The observation area was enclosed in a clear acrylic box and flushed with dry nitrogen to prevent frosting. Images were recorded in ~0.17 °C intervals and stored for post-processing. When a water drop froze, the drop darkened from a nearly transparent, white circle to a fully black circle. An in-house-developed algorithm processed the images to automatically detect potential freeze events. Suspected freeze events were inspected manually and determined to be either a true freeze event, a false positive, or a freeze event induced by drops coming in contact with each other., 18. Based on the video image analysis, the number fractions of droplets frozen and unfrozen relative to the total number of droplets were counted every 0.5 °C., 19. Individual freezing events of the droplets were detected automatically by image processing using homemade LabVIEW program. In the first stage, the program detected the droplets and their diameters by a shape criterion using VISION software. In the second stage, every droplet is surrounded by a square to create array of pixels. The gray level values of the array are analyzed in each frame of the movie and compared to the liquid droplet values. When the droplets froze, the small crystals were scattering more light and the droplet darkens. Hence, the average brightness in the square array decreased and the automatic program recorded this brightness negative peak as a freezing point., 20. We ran 3x7 of pure water (solvent) in the side by side position of solution droplets during the experiment to make sure no pure water droplets started freezing prior to the completion of solution droplets freezing. This simultaneous measurement ensured no freezing emanated from water itself. We discarded the experiment if we observed the freezing event of pure water prior to that of solution droplet., 21. Ice nucleation was determined optically based on the change in droplet brightness when the initially transparent liquid droplets became opaque upon freezing. If the freezing temperature was not obvious for any droplets, the 8-bit grayscale images were assessed on the ImageJ software to determine the temperature of phase shift for suspicious droplets by varying the minimum threshold gray value of 155-175 at the fixed maximum threshold value of 255.